Supplementary Materials for

Multivascular networks and functional intravascular topologies within biocompatible hydrogels

Bagrat Grigoryan*, Samantha J. Paulsen*, Daniel C. Corbett*, Daniel W. Sazer, Chelsea L. Fortin, Alexander J. Zaita, Paul T. Greenfield, Nicholas J. Calafat, John P. Gounley, Anderson H. Ta, Fredrik Johansson, Amanda Randles, Jessica E. Rosenkrantz, Jesse D. Louis-Rosenberg, Peter A. Galie, Kelly R. Stevens†, Jordan S. Miller†

*These authors contributed equally to this work.
†Corresponding author. Email: ksteve@uw.edu (K.R.S.); jmil@rice.edu (J.S.M.)

Published 3 May 2019, *Science* **364**, 458 (2019)
DOI: 10.1126/science.aav9750

This PDF file includes:

Other Supplementary Material for this manuscript includes the following:
(available at science.sciencemag.org/content/364/6439/458/suppl/DC1)

Movies S1 to S5 (.mp4)

Materials and Methods

Development of open-source stereolithography apparatus for tissue engineering (SLATE)

Our custom-designed stereolithography apparatus for tissue engineering (SLATE) is open-source and contains 3 major components that are attached to an aluminum frame: 1) electronics motherboard (RAMBo; UltiMachine, South Pittsburg, TN) for system control *(8)* running Marlin firmware deposited into the open data repository for this work *(39)*; 2) a z-axis with stepper motor linear drive (1 mm/revolution); 3) a 3D printed plastic base with a 45° mirror to reflect the projected images onto the build platform **(fig. S1)**. A build platform containing a glass slide onto which the hydrogels are fabricated is attached onto the Z-stage. The vat consists of a poly(dimethylsiloxane) (PDMS; Sylgard 184, Dow Corning, Midland, MI) coated P100 Petri dish secured by clamps. The PDMS coating prevents sticking of the printed object onto the Petri dish. The base, mirror mount, microcontroller housing, build platform, and Z-platform were 3D printed with an Ultimaker 2 (Ultimaker, Netherlands) in consumer-grade poly(lactic acid) (PLA) plastic filament. Details of the components and 3D models are provided in the **Bill of Materials** in the open data repository for this work *(39)*.

The projection device consists of an Acer H6510BD home theater projector (Acer, San Jose, CA) with a display resolution of 1920×1080 pixels, or a PRO4500 Optical Engine (with a display resolution of 1280×800 pixels), or a PRO6500 Optical Engine (with a display resolution of 1920×1080 pixels) containing a 405 nm LED (Wintech, Carlsbad, CA), attached to a computer for projection of photomasks and motor control. The projector is placed in front of the developed SLATE apparatus and focused to obtain an xy voxel resolution of 38 μm (Acer), 50 μm (PRO4500), or 10 μm (PRO6500).

Design of perfusable vessel architectures

Because vascular networks have evolved to address the metabolic needs of thick tissues by incorporating fractal-like architectures that are efficiently space-filling, mathematical space-filling curves such as the Hilbert curve, Schwarz P surface, and topologies from knot theory were explored to create synthetic analogues. Interpenetrating 3D models utilizing such space-filling curves were designed in an open-source 3D computer graphics software Blender (Blender Foundation, Amsterdam, Netherlands) and adapted from add-ons such as Sverchok (Hilbert curves) and Torus Knot+ (Torus knot models), or in SolidWorks (Dassault Systemes SolidWorks Corp., Waltham, Massachusetts). Intravascular components were also designed either in Blender or SolidWorks.

Photosensitive material synthesis, photorheology, and hydrogel fabrication

Polymer and photoinitiator synthesis

Poly(ethylene glycol) diacrylate (PEGDA; 3.4 kDa, 6 kDa, 10 kDa, 20 kDa, and 35 kDa) was prepared as previously described *(42)*. Briefly, dry poly(ethylene glycol) was reacted with triethylamine and acryloyl chloride in anhydrous dichloromethane under argon overnight. Yields were typically in the range of 80-90% and percent acrylation was ≥ 90%, as verified by ^{1}H NMR for the characteristic peak of the PEG methylene protons adjacent to the acrylate, for batch sizes up to 350 g.

Lithium phenyl-2,4,6-trimethylbenzoylphosphinate (LAP) was prepared as previously described *(43)*. Briefly, dimethyl phenylphosphinite and 2,3,6-trimethylbenzoyl chloride were reacted under argon overnight at room temperature followed by addition of 4 molar excess lithium bromide in 2-butanone. The reaction mixture was then heated to 50 °C to allow formation of a solid precipitate, cooled to room temperature for 4 hrs, followed by filtration with excess amount of 2-butanone and diethyl ether. Yields up to 90% were achieved for batch sizes up to 30 g.

Gelatin methacrylate (GelMA) was synthesized as previously described *(44)*, with slight modifications. Methacrylic anhydride was added dropwise to gelatin dissolved in carbonate-bicarbonate buffer at 50 °C for 3 hrs, followed by precipitation in ethanol. The precipitate was allowed to dry, dissolved in phosphate buffered saline (PBS), frozen at -80 °C, then lyophilized for up to 1 week. GelMA was stored at -20 °C until use.

Photorheology characterization of hydrogels printed with different photoabsorbers

Photorheological characterization of hydrogels was performed using an AR-G2 parallel plate rheometer (TA Instruments, New Castle, DE) equipped with a 20 mm diameter parallel plate geometry and an optics attachment in which a PRO4500 projector was used as the light source. For each sample pre-hydrogel mixture (20 wt% 6 kDa PEGDA with 34 mM LAP and various concentration of dye) was loaded onto the bottom plate and the top geometry was lowered to obtain a gap size of 50 or 100 μm. Four-minute time sweep tests were performed, with an angular frequency of 5 rad/s and 0.1% strain, in which the sample was preconditioned for 30 s and then light was initiated for either a short duration (6-40 s) or long duration (120 s) via the PRO4500 (21.5 ± 1.5 mW/cm^2). We measured the evolution of the storage modulus of pre-hydrogel mixture containing various concentrations of light absorbers: tartrazine (Sigma, St. Louis, Missouri), curcumin (Sigma), anthocyanin (Badmonkey Botanicals, Tacoma, WA), gold nanoparticles (50 nm, nanoComposix, San Diego, CA) **(fig. S4)**.

Photorheological characterization for working curve determination

By using a parallel plate rheometer to maintain a fixed layer height, we quantified the time required for pre-hydrogel samples to achieve their gel point and plotted these values as a

function of layer height and photoabsorber concentration (the resulting scatter plot is known as a working curve). A material reaches its gel point when, under shear deformation, it stores and returns more energy than it loses due to viscous frictional heat, that is when the storage modulus is greater than the loss modulus. For each sample, a pre-hydrogel formulation of 20 wt% 6 kDa PEGDA and 34 mM LAP was used, along with 1.000, 2.255, 3.500, or 5.000 mM tartrazine. The rheometer parallel plates were set to 50, 100, or 200 μm to provide a fixed layer height, and dynamic oscillation was performed on each sample with an angular frequency of 5 rad/s, 10% strain, and 16.4 mW/cm^2) of 405 nm light. Experimental data provided by the rheometer allow the gel point to be detected, which occurs at the exact time when the storage modulus (G', a measure of energy stored during shear deformation) becomes larger than the loss modulus (G", a measure of energy lost during shear deformation). The resulting working curve contains points defined by two independent variables (layer height and tartrazine concentration) and one dependent variable (time to gel point) **(fig. S4)**.

Photorheological characterization of growth and step photopolymerization

We found that tartrazine's photoabsorbent properties enables hollow vessel fabrication in not only PEGDA hydrogels but also in PEG-based thiol-ene hydrogels **(fig. S5D)**. This finding is attractive because thiol-ene photocrosslinking proceeds via step-growth polymerization, which is known to provide less oxygen quenching and faster reaction times when compared to chain-growth polymerization mechanisms like that of PEGDA. Photorheology was therefore performed on single layer gels of PEGDA and PEG-based thiol-ene composition, using the exact set of chemical and light parameters that were originally found to yield hollow vessels during stereolithography **(fig. S5A-C)**. The experimental parameters were as follows: 20 wt% 6 kDa PEGDA or 5.88 wt% 8-arm PEG-norbornene and 4.12 wt% PEG-dithiol (JenKem Technology, Plano, TX); 16.4 mW/cm^2; 50 μm layer height. These samples were placed on the rheometer and exposed to the appropriate duration of light under dynamic oscillation (5 rad/s, 10% strain), providing real-time quantification of hydrogel stiffening (i.e. reaction progress). In separate experiments, the PEG-based thiol-ene samples were exposed to sequential, discrete illumination periods of 3 s each with 20 s intervals between them.

Hydrogel fabrication by projection stereolithography

For fabrication of acellular monolithic gels, pre-hydrogel mixtures were prepared containing 20 wt% 6 kDa PEGDA (unless otherwise stated), 34 mM LAP, and photoabsorber concentration based on desired layer thickness. The pre-hydrogel mixture was transferred onto the PDMS coated Petri dish placed below the build platform, which contains a bonded glass slide onto which the cured gel would attach, was lowered to the first fabrication layer position, and fabrication was managed with Creation Workshop software (http://www.envisionlabs.net/), which controls the apparatus by sending GCode commands for vertical movement of the build platform, and images to the projector, which projects a sequence of photomasks based on the

imported 3D model. After printing is completed, the 3D fabricated hydrogel is removed from the glass slide of the build platform with a razor and equilibrated in deionized (DI) water or PBS with multiple washes.

For continuous fabrication of acellular hydrogels, the build plate was slowly moved upwards, without lowering of the build plate in between layers, during continuous projection of sliced images **(fig. S5E)**.

For visualization of topologies, we perfused microfil (Flow Tech Inc, Carver, MA) containing different color dyes into the open channels of fabricated topologies and allowed the microfil to set before taking photographs **(Fig. 2A-D)**. Macro photographs were captured with a Canon 5DSR camera (Canon, Tokyo, Japan) and MP-E 65 mm macro lens or EF 100 mm macro lens in RAW mode (50 megapixel) under room lighting or with an Ikan LYRA LED array (Ikan, Houston, TX) or with an Einstein flash (Paul C. Buff, Nashville, TN). Video was captured with the same equipment or with a Sony mirrorless A7SII camera (Sony, Tokyo, Japan) with a Sigma adapter (Sigma, St. Louis, MO) for the MP-E 65 mm lens. Since microfil contains radiopaque agents, we used microcomputed tomography (μCT) to investigate pattern fidelity. Swollen hydrogels with microfil perfused into the channels were scanned at 0.6 degree steps at 9 μm voxel resolution on a SkyScan 1272 μCT scanner (Bruker, Billerica, MA) equipped with a 11 megapixel camera (XIMEA, Lakewood, CO). Volumetric visualization of scanned hydrogels was achieved by importing reconstructed images (obtained by nRecon Reconstruction software, Bruker, Billerica, MA) into Imaris Image Analysis Software (Bitplane, Zurich, Switzerland).

Circularity measurements

By adding photoabsorbers to the aqueous pre-hydrogel solution, circular or square channels can be fabricated as patent channels **(fig. S3)**. To determine the impact of print layer thickness on fidelity of circular vessels, gels containing a single 1 mm diameter horizontal channel were fabricated using a layer thickness of 25, 50, 100, or 200 μm. Hydrogels were fabricated out of 20 wt% 6kDa PEGDA, tartrazine as the photoabsorber, and 34 mM LAP. FITC-dextran was also incorporated into the aqueous pre-hydrogel print solution prior to fabrication so that the geometry of the resulting channel could be observed using a Nikon Eclipse Ti inverted epifluorescent microscope (Nikon Instruments Inc., Melville, NY) with a Zyla 4.2 sCMOS camera (Andor, South Windsor, CT). All gels were allowed to swell in DI water for 24 hrs prior to image acquisition.

Fluorescence images were analyzed in ImageJ (National Institutes of Health (NIH), Bethesda, Maryland) using the freely available Hull and Circle plugin (version 2.0a, NIH) to determine the circularity of each fabricated channel. Circularity was measured by selecting a region of interest around the channel and instructing the plugin to calculate circularity using its default algorithm. Documentation of this algorithm is available online (https://imagej.nih.gov/ij/plugins/hull-circle.html). Circularity of the channel, C, is then

computed according to:

$$C = \frac{4\pi A}{p^2} \tag{1}$$

where A = area of the convex hull; p = perimeter of the convex hull. Note that in this equation, the circularity of a perfect circle is equal to 1, and the circularity of a rectangle with infinitely high aspect ratio is equal to 0.

Tartrazine release

To measure the release rate of tartrazine from printed hydrogels, three groups of two gels were fabricated (20 wt% 6 kDa PEGDA, 50 μm layer height) using the geometry shown in **(fig. S2A)**. One gel from each group was then added to 500 μL of DI water. At 0.5, 1, 2, 4, 8 and 24 hours, the water was collected, the volume was measured (since the gels swell and absorb water over time), and the water was replaced with 500 μL of fresh DI water. To calculate the amount of tartrazine released at each time point, the absorbance of each sample at 430 nm was compared to that of a standard curve. Next, to determine the amount of tartrazine remaining in each gel after the fabrication process (tartrazine undergoes photo-chemical degradation when exposed to light and free radicals *(45)*), the second gel from each group was added to 1 mL of 1 M sodium hydroxide and degraded over 48 hours **(fig. S4B)**. The absorbance of the degraded gels was then compared with a standard curve of tartrazine that had been exposed to the same pH conditions. The amount of tartrazine remaining in printed gels was then used to calculate the total percentage of tartrazine released from the gels over time.

Vessel compliance measurements

For investigating compliance of channels within our generated gels, we fabricated hydrogels containing a straight, horizontal channel (model info: diameter: 1.5 mm; length: 20 mm) out of 20-60 wt% PEGDA of molecular weights 3.4 kDa, 6 kDa, and 1:1 mixture of 6:35 kDa **(fig. S6)**. After equilibrium swelling, the gel was connected to our open-source pneumatic system whose designs are given in our open data repository for this work *(39)*. We ensured proper fluidic connections. We calculated compliance of channels by measuring the change in internal channel diameter through fast acquisition of brightfield images as the pressure was ramped from 80 to 120 mmHg. Images were obtained on an optical stereo microscope (SteREO Discovery.V8; Zeiss, Oberkochen, Germany) equipped with a Zyla 4.2 sCMOS camera (Andor, South Windsor, CT). Internal diameter of the channels was measured using NIS Elements software (Nikon Instruments Inc., Melville, NY). Compliance, C, was measured as previously reported for tissue-engineered blood vessels *(46)*:

$$C = \frac{(d_{120} - d_{80})/d_{80}}{\Delta P} \tag{2}$$

where d_{120} = diameter of the channel at 120 mmHg; d_{80} = diameter of the channel at 80 mmHg; ΔP = pressure difference (in this case: 120 mmHg - 80 mmHg = 40 mmHg).

Intra and Intervascular Transport Characterization

Mixing efficiency of static mixers

Static mixers were designed based on the Armeniades static mixer *(47)*, which contains 150 μm thick fins with 180° twists in alternating clockwise/counterclockwise directions **(Fig. 1A)**. The static mixers were printed with tartrazine as the photoabsorber with 80 wt% 6 kDa PEGDA at 25 μm layers. To assess mixing efficiency, fluorescent dyes (2 mg/mL 150 kDa FITC-dextran and 1 mg/mL 70 kDa Rhodamine-dextran) were mixed in a 9:1 glycerol:water solution, to reduce the Reynolds number to 0.002, and flowed into the mixers through a Y-junction at rates of 15 μL/min using a syringe pump (Harvard Apparatus, Hollison, MA). Images of the gels were then acquired using a Nikon Eclipse Ti inverted epifluorescence microscope and the mixing ratio was calculated in MATLAB (MathWorks, Natick, MA) by computing the percent overlap between the two normalized fluorescence intensity profiles at the gel outlet, immediately following the last fin element **(fig. S7)**.

Flow visualization of venous valves

The bicuspid valve design was adapted from a tricuspid heart valve model available through the NIH 3D print exchange (Model ID: 3DPX-000452) *(48)*, where the geometry was altered to a bicuspid structure as is typically found in venous valves. The model was then scaled down to approximately 2 mm in diameter, roughly the size of the human saphenous vein **(Fig. 1B)** *(49)*. Valve models were fabricated using 20 wt% 6 kDa PEGDA and a layer height of 50 μm. To assess functionality of the printed valves, gels were allowed to swell overnight before being connected with our custom pneumatically driven pressure system.

Microparticle image velocimetry (μPIV) quantified the flow field passing through the printed biscuspid valve geometry **(Fig. 1B)**. Polystyrene beads labeled with the Nile Red fluorophore (mean diameter of 1.95 μm, peak excitation: 550 nm, peak emission: 640 nm, Spherotech Inc., Lake Forest, IL) were suspended in phosphate buffered saline at a dilution of 1:500. Particles were illuminated with dual pulse Nd:YAG lasers (125 mJ/pulse, 15 Hz, 532 nm, Dantec Dynamics, Skovlunde, Denmark) with pulse width set to 50 μs for a total testing duration of one second. A 4× objective on a Nikon Ti-E inverted microscope was used to visualize the beads, with the focal plane set at the midpoint of the total valve height. A high-speed, high-resolution, double-frame CCD camera (FlowSense EO, 2048×2048 pixel, 7.40 μm/pixel, 53%-quantum efficiency, Dantec Dynamics, Skovlunde, Denmark) captured the flow illuminated by the dual-pulsed lasers. Acquired images were analyzed using Dynamic Studio software (Dantec Dynamics, Skovlunde, Denmark) using an adaptive PIV algorithm, which optimizes the interrogation area based on particle number. A detailed explanation of this method can be found in previous studies *(50)*. An initial interrogation area of 32×32 pixels was

input into the adaptive PIV algorithm. Post-processing of the measured velocity vectors into a contour/arrow plot was performed using MATLAB software **(Fig. 1B)**.

RBC oxygenation studies

Human packed red blood cells (human RBCs, type O negative, Interstate Blood Bank, Memphis, TN) were stored at 4 °C until use, and used within 7 days of arrival. RBCs were warmed to room temperature before use and was mixed in a 3:2 ratio with PBS to lower the hematocrit to 40%, as verified by a blood gas analyzer (ABL-80 CO-OX Flex, Radiometer, Brea, CA). Deoxygenated RBCs were utilized with $pO_2 \leq 40$ mmHg and $sO_2 \leq 45\%$.

For initial investigation in oxygen delivery between two channel networks, we designed and fabricated a hydrogel out of 20 wt% 6 kDa PEGDA which contains two interpenetrating networks: 1) a serpentine vessel; 2) a helix network that wraps around the serpentine network (model size = 34×17×6 mm (total volume: 3.5 mL); serpentine channel diameter = 0.6 mm; helix channel diameter = 0.5 mm; intervessel distance = ~0.3 mm; **(Fig. 2E,F)**). We continuously perfused the deoxygenated RBCs (at 15, 25, and 35 μL/min) through one vessel network while humidified nitrogen or oxygen was continuously perfused through the other network at 7 kPa **(fig. S8)**.

We also designed and fabricated a hydrogel (20 wt% 6 kDa PEGDA) based on the Weaire-Phelan space-filling foam model (model volume = 0.8 mL; vascular channel diameter = 0.35 mm; spacing between vascular and airway components = ~0.35 mm; **(fig. S9A,B)**). The fundamental Weaire-Phelan (WP) unit cell *(35)* is composed of 2 dodecahedron and 6 tetrakaidecahedron cells which can be tessellated in 3D to fill space. We first produced the fundamental unit of the foam structure from the individual dodecahedron and tetrakaidecahedron cells of equal volume. To generate the vascular component of the model, we removed all faces and the internal edges and vertices, and utilized the remaining topology as a vascular skeleton. We skinned the skeleton with a polygonal mesh and then applied Catmull-Clark smoothing to produce cylindrical channels along the edges of the model with intervessel junctions located at each vertex. To generate the airway component of the model, we took the unmodified fundamental Weaire-Phelan unit and scaled the faces along local face normals in a manner such that the airway was nested inside the vasculature. We then designed independent fluidic connections to the vasculature and airway. Finally, we performed a boolean subtraction of these perfusable channels from a solid volume, generating our final 3D model for printing. We continuously perfused the deoxygenated RBCs through the vascular vessel while oxygen was cyclically perfused through the airway network from 0 to 10 kPa at 0.5 Hz **(Fig. 3 and Movie S3)**.

For the algorithmic lung-mimetic design **(fig. S9F)**, we first designed the model airway by fusing multiple spheres in a radially symmetric fashion. We next offset the airway topology to generate the vascular surface topology, which was then tessellated, skelatonized, and then skinned to produce a voronoi vascular topology. We performed a boolean subtraction of the original airway and the tesellated voronoi vascular topology from a solid volume to generate

the final 3D model for printing. For the nitrogen and oxygen cycling studies, we continuously perfused the deoxygenated RBCs at 10 μL/min through the vascular vessel while nitrogen or oxygen was cyclically perfused through the airway network from 0 to 24 kPa at 0.5 Hz **(Fig. 3 and Movie S4)**. Samples were analyzed every 15 minutes.

Gels were allowed to reach equilibrium in DI water for up to 5 days before performing oxygenation studies. For each gel, we ensured proper fluidic connections with flexible plastic tips (Nordson Corporation, Westlake, OH), using cyanoacrylate glue as necessary to avoid leaks. Before RBC perfusion was initiated in the serpentine-helix gel, the channels were flushed with air to remove residual water inside channels. Before RBC perfusion was initiated into the bioinspired models, gas was cycled into the airway to remove residual water before the airway outlet was sealed. Our open-source pneumatic system was used for all studies.

The perfused blood was collected from the outlet of the corresponding vascular channel into a capillary tube (Clinitubes, Radiometer, Brea, CA) and pO_2 (partial pressure oxygen), pCO_2 (partial pressure carbon dioxide), sO_2 (oxygen saturation), tHb (total hemoglobin), O_2Hb (oxyhemoglobin), HHb (deoxyhemoglobin), COHb (carboxyhemoglobin), and MetHb (methemoglobin), and hematocrit values were obtained using the blood gas analyzer.

Computational models

Computational models for the static mixer and Weaire-Phelan airway were developed using COMSOL Multiphysics 5.2a (COMSOL Inc., Burlington, MA). The static mixer geometry was imported into COMSOL using LiveLink for Solidworks, where the original geometry was scaled up by a factor of 1.3 to account for equilibrium swelling of the hydrogel. The model was solved using the single phase laminar flow module and stationary solver incorporating the parameter values described in **Table S1 (Fig. 1A)**.

To investigate gel distortion when pneumatic air pressure was introduced in the airway as observed in the bioinspired alveolar model, we designed a simple rotationally symmetric polygon with alternating convex and concave regions, which represents the airway, with circular vessels (300 μm) equidistant from these regions. The structural mechanics module was applied using the stationary solver incorporating the parameters described in **Table S1** and an interior boundary ranging from 500-5,000 Pa **(fig. S9E)**.

A further computational simulation to investigate the relationship between distension and local curvature was explored in HARVEY **(Fig. 3D)**, a computational hemodynamics application *(40)*. Designed for large-scale parallel efficiency, HARVEY is primarily written in C++ and parallelized with MPI. Simulations were conducted on the Duke Compute Cluster.

The hydrogel, air, and blood are modeled as Newtonian fluids defined on a fixed Cartesian lattice with Eulerian variables. The assumption of Newtonian behavior is reasonable for PEG-based hydrogels at low shear rates *(52)*, though it remains a simplification for blood. Flow is simulated with the lattice Boltzmann method, which solves the weakly compressible Navier-Stokes equations and is based on the Boltzmann equation of kinetic theory *(53)*. The experimental system was also simplified by removing inlets and outlets from the airway and

	Parameter	Value	Unit		Parameter	Value	Unit
Static Mixer	Density of liquid	1236.1 *(51)*	kg/m^3	**Alveolar Inspired Model**	Young's Modulus	20	kPa
	Dynamic viscosity	0.26048 *(51)*	Pa·s		Poisson's Ratio	0.49	
	Inlet velocity	1.274	mm/s		Density	1000	kg/m^3
					Load on interior airway	500-5000	Pa

Table S1: Parameters used in computational models.

vasculature, in keeping with the focus on the influence of airway expansion on the surrounding vasculature. Instead, the density of the fluid inside the airway was made to increase in time, in order to approximate the behavior of a compressible fluid flowing into the airway and causing it to expand.

Conversely, the airway and blood vessel walls are modeled as zero-thickness, massless membranes. The membranes resist deformation according to a linear visco-elastic constitutive law and bending resistance, generalizing the model proposed in *(54)* and extending it to three-dimensions. The membranes are represented numerically by triangulated surface meshes described by Lagrangian variables. The surface meshes are based on the experimental topologies and refined to avoid numerical 'leakage' of fluid through the membranes. Extending our recent work with deformable cells *(55)*, HARVEY uses the immersed boundary method to describe the interaction of the deformable airway and vessel walls with the surrounding fluids. The immersed boundary method couples the Lagrangian description of the deformable walls with the Eulerian description of the fluids using smoothed Dirac delta functions *(56)*. Developed by Peskin to model blood flow in the heart *(57)*, the immersed boundary method has been applied to model the fluid-structure interaction of blood with deformable vessel walls *(58)*.

The resulting fluid-structure interaction in HARVEY is performed in the following manner. Using the immersed boundary method, the positions of the airway and vessel walls are updated by the local fluid velocity using a no-slip condition. The resistance of these deformable walls to deformation and velocity is computed as force densities defined at each vertex of the surface mesh. The resulting forces are 'spread' onto the surrounding fluid domain by the immersed boundary method. Finally, the velocities on the fluid domain are updated with these external forces using the lattice Boltzmann method and the simulation proceeds to the next time step.

Cell Printing

For fabrication of cellularized gels, the stereolithography apparatus was placed in a tissue culture hood for printing under sterile conditions using sterilized PDMS-coated dishes, build platforms, and 0.22 μm filtered pre-hydrogel solutions.

Motivated by the therapeutic potential of readily available cryopreserved mammalian cells stored in cell banks, we sought to develop a rapid biomanufacturing workflow in which cryopreserved cells can be incorporated into perfusable hydrogels immediately after thaw

(fig. S10A). With this approach, mammalian cells from liquid nitrogen storage (-196 °C) are thawed to room temperature, mixed with pre-hydrogel solution, and dispensed into a sterile Petri dish vat for bioprinting. Crucially, our custom stereolithography apparatus for tissue engineering (SLATE) **(fig. S1)** fits entirely inside common biosafety cabinets with sufficient room for cell handling. Although SLATE fabrication is rapid (at up to 12 mL/hr with voxels of 250 pL), mammalian cells typically settle out of suspension within tens of seconds. To prevent cells from settling and facilitate automated bioprinting, we added xanthan gum—a natural, biocompatible, shear-thinning carbohydrate *(59)* utilized in the food industry—to the pre-hydrogel solution. Hydrogels composed of tens of layers can be printed in a few minutes, and mammalian cells are uniformly distributed **(fig. S11A,B)**.

Densely populated tissues pose significant challenges for nutrient delivery and present difficulties for microscopy which could otherwise be used to interrogate cellular function. To this end, we developed a modified luminescence assay with mammalian cells that constitutively express firefly luciferase (Luc2P) to non-invasively assess cellular activity. The entire workflow from the thaw of cryopreserved cells, through SLATE fabrication, and perfusion of patterned hydrogels with cellular growth media and luciferin substrate is completed in less than one hour **(fig. S10A)**. Because the firefly luciferase enzyme requires stoichiometric availability of ATP and oxygen for chemiluminescence *(60)*, we hypothesized that delivery of oxygenated media into vascular conduits would boost the light output of Luc2P cells that could access oxygen from the perfusate. We observed significantly improved light output from cellularized hydrogels perfused with luciferin media containing oxygenated RBCs (pO_2 > 100 mmHg, sO_2 > 90%) compared to deoxygenated RBCs (pO_2 < 40 mmHg, sO_2 < 45%) **(fig. S10B,C and Movie S5)**. Further, we observed this assay was readily able to discriminate between a variety of cellular densities and media perfusion rates **(fig. S11)**.

Luminescence screening

For non-invasive, non-destructive imaging of cellularized gels, HEK293T cells transduced to constitutively express mCherry and Luc2P were used. First, frozen stocks of cells were generated at 5×10^7 per cryovial. For fabrication of gels with cells directly from liquid nitrogen storage, cell vials were thawed, resuspended in media, then centrifuged to obtain a pellet. The pre-hydrogel mixture was added to the cell pellet, mixed well to reduce clumping of cells, the mixture was transferred to a sterile PDMS-coated dish, and printing was initiated.

To aid in homogeneous distribution of cells throughout the height of the gel, xanthan gum (Sigma), a natural thickening agent, was added into the pre-hydrogel solution to reduce the settling time of cells **(fig. S11)**. We found that addition of low amount of high molecular weight xanthan gum (< 0.1 wt%) allowed the fabrication of hydrogels with a homogeneous cell distribution along the height of the gel. Additionally, glycerol was added into the pre-hydrogel solution to reduce cell clumping.

After printing was completed, the gels were rinsed with media to remove leftover printing solution, removed from the glass slide of the build platform, and transferred into a Petri dish

containing media. After 15 minutes incubation the gel was then placed into a sterile custom designed chamber for perfusion studies. Fluidic connections were obtained by inserting flexible plastic tips (Nordson Corporation, Westlake, OH) into the inlet/outlet of the gel. The chamber, containing the gel, was transferred into an IVIS Lumina K (PerkinElmer, Waltham, MA) for imaging. Bioluminescence images were taken every 5 minutes for 3 hrs while cell culture media containing luciferin (0.15 mg/mL) was perfused through the channel of the gel. All gels fabricated for luminescence screening were composed of 20 wt% 6 kDa PEGDA with 17 mM LAP and tartrazine as the photoabsorber.

For assessing the effect of cell density and luciferin flow rate on the total light output of fabricated hydrogels, we designed and fabricated a hydrogel containing a horizontal channel (model size = 32×14×3 mm (total volume: 1 mL); channel diameter: 0.8 mm). We tested hydrogels with cell densities of 5×10^6, 1×10^7, 2.5×10^7, and 5.0×10^7 cells/mL while perfusing the luciferin containing media at 50 μL/min. Additionally, we measured the total luminescent output of hydrogels containing cells at 2.5×10^7 cells/mL with luciferin inflow rates of 10, 25, and 50 μL/min **(fig. S11)**. Before luciferin injection, PBS was perfused into the gel to ensure that no air bubbles were present within the channel of the gel.

To investigate the change in luminescent output of cells exposed to oxygenated vs. deoxygenated RBCs, we fabricated a hydrogel model containing a serpentine vessel (model size = 32×14×3 mm (total volume: 1 mL); channel diameter: 0.8 mm) **(fig. S10B,C)**. We fabricated these gels at 2.5×10^7 cells/mL. Instead of perfusing the channel with standard cell culture media containing luciferin, we mixed RBCs with media at a ratio of 3:2 to lower the hematocrit to 40% before addition of luciferin (0.15 mg/mL final concentration). The RBC-media mixture used to perfuse the hydrogels was either deoxygenated ($pO_2 < 40$ mmHg, $sO_2 < 45\%$) or oxygenated ($pO_2 > 100$ mmHg, $sO_2 > 90\%$) and was perfused into the inlet of the gel via a syringe pump (Harvard Apparatus, Hollison, MA) at 10 μL/min. Before luciferin injection, PBS was perfused into the gel to ensure that no air bubbles were present within the channel of the gel.

hMSC 2D Viability

For 2D studies, human mesenchymal stem cells (hMSCs; RoosterBio, Frederick, MD) at passage 3-5 were seeded into a 48 well plate at 3000 cells/cm^2 and allowed to incubate overnight. Then, cells were incubated with LAP (0-50 mM) and tartrazine (0-10 mM) for 20 or 60 minutes, rinsed with PBS, then stained using Live/Dead (Life Technologies, Carlsbad, CA) according to the manufacturer's instructions **(fig. S13)**. Cells treated with 70% ethanol prior to staining served as negative controls. Fluorescence imaging was performed on a Nikon Eclipse Ti inverted epifluorescent microscope (Nikon Instruments Inc., Melville, NY) equipped with a Zyla 4.2 sCMOS camera (Andor, South Windsor, CT). Live and dead cells were quantified either manually or using CellProfiler (http://cellprofiler.org/).

hMSC 3D Viability

For 3D hMSC encapsulation studies, we fabricated cylindrical hydrogels (diameter = 6 mm; height = 1 mm) of different material compositions to assess viability and differentiation (with xanthan gum in the pre-hydrogel solution to prevent cell settling) **(fig. S13)**. For short-term cell viability determination, we fabricated gels out of 15 wt% GelMA along with a mixture of 12 wt% 6 kDa PEGDA + 8 wt% GelMA (with or without tartrazine) with hMSCs (p3-4) at 1×10^6 cells/mL. Mixtures of PEGDA and GelMA have been mechanically characterized and reported in previous studies *(61, 62)*. To aid in homogeneous distribution of cells throughout the height of the gel, xanthan gum (Sigma), a natural thickening agent, was added into the pre-hydrogel solution to obtain a neutrally buoyant suspension. The gels were rinsed with media, removed from the build platform, and transferred into a well plate. For hydrogels fabricated with tartrazine, media was replaced 3 times within the first 2 hours of incubation. After either 2 or 24 hr incubation gels were rinsed with PBS and viability of encapsulated cells was determined using Live/Dead assay (Life Technologies, Carlsbad, CA) according to the manufacturer's instructions. Gels treated with 70% ethanol prior to staining served as negative controls. Fluorescent imaging was performed on a Nikon Eclipse Ti inverted epifluorescent microscope (Nikon Instruments Inc., Melville, NY) equipped with a Zyla 4.2 sCMOS camera (Andor, South Windsor, CT). Live and dead cells were quantified using Nikon NIS Elements software.

hMSC osteogenic differentiation

For 3D osteogenic differentiation studies, we fabricated similar cylindrical hydrogels out of similar material composition as the 3D viability experiments, using 10×10^6 cells/mL. After gels were transferred to a well plate, growth media was added to all wells and placed in TC incubator. Media was replaced 4 times within the first 24 hrs. After 3 days in growth media, the media of half of the fabricated gels was changed to osteogenic media (growth media supplemented with 10 mM β-glycerophosphate and 50 μg/mL L-ascorbic acid). After 30 days of incubation in osteogenic media, gels were rinsed with PBS, fixed in 4% paraformaldehyde, rinsed in DI water, and incubated in 2% Alizarin Red Solution for 3 hours *(63)*. Stained gels were rinsed with DI water until no further dye could be removed. Gels were incubated in 10% acetic acid overnight to solubilize the dye, then diluted 5-fold in DI water. Dye concentration was obtained by first running an absorbance sweep to determine the maximum absorbance wavelength (found to be at 424 nm), then obtaining absorbance scan of all samples at that wavelength (Tecan microplate reader; Tecan, Mannedorf, Switzerland) **(fig. S13)**.

We then generated perfusable hydrogels containing a single 1 mm diameter horizontal channel with encapsulated hMSCs at 10×10^6 cells/mL using a formulation composed of a mixture of PEGDA and GelMA. Printed gels were rinsed with sterile PBS to wash leftover cells and printing formulation, transferred into a dish and submerged in growth media for 10 minutes. Then the gels were transferred into a sterile chamber, fluidic connections were obtained and ensured, and set up for perfusion culture with perfusion of growth media at 10 μL/min. After overnight perfusion of growth media, the perfused growth media was replaced

with osteogenic or adipogenic media (StemPro kit) for some of the hydrogels. Hydrogels were then perfused for 14 days, with replenishment of media every 2 days. At the end of 14 days of differentiation media perfusion, gels were rinsed with PBS, fixed in 4% paraformaldehyde overnight at 4 °C, and prepared for cryosectioning. Hydrogels were oriented in the cryomolds so that cryosectioning would yield sections in which the horizontal channel is oriented upwards. Sections were stained for lipid droplets with Oil Red O (Sigma) and for alkaline phosphatase (ALP), using Fast Blue RR Salt/Naphtol (Sigma). hMSC differentiation media for perfused gels involved StemPro Adipogenesis Differentiation Kit or StemPro Osteogenesis Differentiation Kit (Thermo Fisher Scientific, Waltham, MA).

Cellular alveolar model

Motivated by our earlier presentation of the gas-exchange behavior of our generated multi-vascular hydrogels, we designed a simplified adaptation of the alveoli, the distal component of the lung. Here, the alveoli are represented as a fusion of spheres, which is a closer approximation to the native morphological structure of alveoli. We then incorporated a proximate yet independent branched vessel network, which envelops the airway topology, to construct a vascular model of the alveoli. While not at scale, the merged spheres topology represents the alveolus while the surrounding branched vessel networks represents the proximate capillaries found in the distal end of the native lung.

Human lung epithelial cells (A549, ATCC, Manassas, VA) were cultured in F-12K media (ATCC) with 10% (v/v) FBS (Atlanta Biologicals). Fluorescent A549 cells were generated using hEF1α-H2B-mVenus-IRES-mCherry third generation lentiviral construct following our previously reported protocol *(64)*. Human lung fibroblasts (IMR-90, ATCC) were cultured in EMEM media (ATCC) with 10% (v/v) FBS (Atlanta Biologicals). Media for hydrogels which underwent perfusion culture was supplemented with 1%(v/v) penicillin-streptomycin.

IMR-90 fibroblast containing hydrogels were fabricated at 10×10^6 cells/mL using a formulation composed of a mixture of PEGDA and GelMA **(fig. S12)**. These hydrogels were transferred into a sterilized 3D printed plastic housing chamber which contains ports for fluidic tips. Fluidic tips were primed with sterile PBS and the tips, connected to a sterile syringe, were gently inserted into the gel chamber and then into the inlet and outlet portions of the hydrogel. Proper fluidic connection was ensured by injecting sterile PBS and visibly verifying absence of leakage into the gel chamber housing. The airway and vascular vessels were perfused with EMEM media at 20 μL/min. After overnight perfusion, perfusion of the airway vessel was stopped so that the airway can be connected to our open-source pneumatic system, using air as the gas source. Sterile tubing from the pneumatic system was routed into the incubator and connected to a humidifying chamber. Humidified air was connected to the inlet of the airway channel for all gels. Before the connection to the fluidic tip inserted into the airway, each gel was connected to its own low-pressure gauge (Kodiak Controls, Romeoville, IL). In between the pressure gauge and the airway inlet fluidic tip, a 0.4 μm filter was placed. The airway outlet was capped. The airway channel was cyclically ventilated from 0-0.5 PSI at 0.05 Hz,

unless otherwise noted. The vascular channel was perfused at 20 μL/min with EMEM media for 5 days and then fixed, cryoembedded, cryosectioned, and stained with Hoechst to visualize cell nuclei.

In studies involving A549 seeded cells into hydrogels containing IMR-90 cells, these co-culture gels were achieved by first printing the hydrogel with IMR-90 cells, connecting to perfusion culture overnight and perfusing EMEM media through the vascular and airway channels, then removing the gel from perfusion, performing our standard seeding workflow, as described below.

For seeding cells into 3D architectures, we transferred equilibrated gels into a sterilized FDM printed housing chamber which contains ports for fluidic tips. Fluidic tips were primed with sterile PBS and tips, connected to a sterile syringe, were gently inserted into the gel chamber and then into the inlet and outlet portions of the gel. Proper fluidic connection was ensured by injecting sterile PBS and visibly verifying absence of leakage into the gel chamber housing. Cells were resuspended at desired concentration, typically at 10×10^6 cells/mL in media, and transferred into a syringe via 18GA syringe needle, ensuring no air bubbles present in the syringe. The syringe was then carefully connected to the fluidic tip inserted into the inlet portion of the printed gel. The cells were then adequately injected into the gel until droplets of cell suspension were dripping out of the gel outlet fluidic tip. The outlet fluidic tip was capped, and the chamber was transferred into a incubator. Fluidic perfusion to the vascular channel was resumed and the seeding protocol was initiated. The cell seeding workflow involved keeping the gel upright for 10 minutes, then rotating 180 degrees and allowing to sit for 15 minutes, then rotating onto one side (90 degree rotation after inverting the gel) of the gel for 15 minutes, followed by allowing the gel to incubate onto the other side (180 degrees rotation after the previous rotation step) for 15 minutes. This procedure was followed a total of two times to provide cells with sufficient time to attach onto the printed architectures. Then, the gel was transferred back into the cell culture hood and the syringe at the inlet site and the cap at the outlet side were carefully removed. A syringe containing sterile PBS was connected to the inlet fluidic tip and 3 mL of PBS was injected gently into the channel to remove unattached cells. Then, the airway vessel was connected to peristaltic tubing and a media bag, transferred back into the incubator, and connected to a peristaltic pump for dual vascular and airway perfusion culture. The vascular channel was perfused at 20 μL/min with EMEM while the airway vessel was perfused at at 5 μL/min. After overnight perfusion, perfusion was stopped, the gels were fixed, cryoembedded, cryosectioned, and stained with Hoechst to visualize cell nuclei.

Liver work

Cell Culture

Primary human umbilical endothelial cells (HUVECs; Lonza; passages 4 to 7) were maintained on dishes in EGM-2 (Lonza). Normal human dermal fibroblasts (NHDFs; Lonza; passages 4 to 9) were cultured in DMEM with 10% (v/v) FBS (source) and 1%(v/v) penicillin-streptomycin.

Rat Hepatocyte Isolation and Culture

Rat primary hepatocytes were isolated as described previously *(65–68)* and maintained in high-glucose DMEM containing 10% (vol/vol) fetal bovine serum (Gibco), 1% (v/v) ITS supplement (insulin, transferrin, sodium selenite; BD Biosciences), 7 ng/mL glucagon (Sigma), 0.04 μg/mL dexamethasone (Sigma) and 1% penicillin-streptomycin (pen-strep, Invitrogen).

Fabrication of Engineered Hepatic Tissues

Engineered hepatic tissues were fabricated in a three-step process. First, hydrogel carriers were printed from either 30 wt% 6 kDa PEGDA, a mixture of 7.5:7.5 wt% 6 kDa PEGDA:GelMA, or a mixture of 3.25 wt% 3.4 kDa PEGDA + 10 wt% GelMA at 50 micron layer thickness. Gels were rinsed and incubated in PBS for 24 hrs prior to cell seeding. Second, to populate hepatic tissues with endothelial cell (EC) cords, HUVECs were suspended at a density of 10 million HUVECs/mL in neutralized liquid collagen (2.5 mg/mL) (Corning) *(38)*. HUVEC-collagen slurry was pipetted into open channels. Constructs were incubated in EGM-2 media for 4 hours to allow for cord formation. Third, to create hepatic aggregates, rat primary hepatocytes were plated in AggreWell micromolds (400μm square AggreWell micromolds, Stem Cell Technologies) along with NHDFs at a 1:1 ratio and incubated overnight *(38)*. Following EC cord formation, hepatic aggregates (100 hepatocytes and 100 dermal fibroblasts per aggregate) were suspended in either fibrin (10 mg/mL) or 5 wt% GelMA at a concentration of 45,000 aggregates/mL casting suspension and pipetted into the hepatic tissue infill space.

In Vivo Implantation of Engineered Tissues

All surgical procedures were conducted according to protocols approved by the University of Washington Animal Care and Use Committee. Female NCr nude mice aged 8-12 weeks old (Taconic; **Fig. 4A-D**) or male Fah-/- backcrossed to NOD, Rag1-/-, and Il2rg-null (FNRG) mice aged 30-40 weeks old (Yecuris) **(Fig. 4E-G)** *(38)* were anesthetized using isoflurane, and the engineered tissue constructs were sutured to the perigonadal fat pad. The incisions were closed aseptically, and the animals were administered buprenorphine (0.1 mg/ml) every 12 hours for 3 days after surgery. NTBC was withdrawn from the animals' drinking water immediately after tissue implantation and for 14 days after implantation.

In Situ Imaging

To enable non-invasive imaging of hepatocyte function, primary hepatocytes were transduced with a lentiviral vector expressing firefly luciferase under the albumin promoter (pTRIP.Alb.IVSb.IRES. tagRFP-DEST, provided through a Materials Transfer Agreement with Charles Rice, The Rockefeller University) as previously described *(41)*. For viral transduction, concentrated virus was diluted 1:5 in hepatocyte medium containing HEPES

buffer (20 mM; Gibco) and polybrene (4 μg/ml; Sigma) in 6-well ultra-low attachment plates (Corning) for 6 hrs. Prior to bioluminescence imaging, mice were injected intraperitoneally with 250 μL of D-luciferin (15 mg/mL; GoldBio) and imaged using the IVIS Spectrum In Vivo Imaging System (Xenogen) and Living Image software (Caliper Life Sciences) after 14 days of implantation.

Tissue Harvesting, Processing, and Histology, and Immunohistochemistry

Animals were sacrificed at the termination of the experiment (10-14 days) following bioluminescence imaging. Tissues were harvested from the intraperitoneal space and fixed in 4% (v/v) paraformaldehyde for 48 hours at 4 °C, incubated in OCT embedding medium (Fisher) for 24 hr at 4 °C, flash-frozen in dry-ice ethanol slurry and sectioned using a cryostat (5 μm) for immunohistochemical analysis.

For gross visualization of tissue, sections were stained with hematoxylin and eosin. For identification of primary rat hepatocytes, sections were first permeabilized with 0.1% Triton-X, blocked with 1.5% normal donkey serum and immunostained with primary antibodies against cytokeratin-18 (rabbit, 1:100; Abcam) followed with species-appropriate secondary antibodies conjugated to (Alexa Fluor 594). To determine graft size, we used Adobe Photoshop to quantify the number of cytokeratin-18 positive pixels in each graft. For identification of mouse red blood cells, sections were permeabilized with 0.1% Triton-X, blocked with 1.5% normal donkey serum and immunostained with primary antibodies against Ter-119 (rat, 1:100; BD Pharmingen) and visualized with species appropriate secondary antibodies conjugated to Alexa Fluor 488. Images were obtained using a Nikon A1R confocal at the Garvey Imaging Lab in the Institute for Stem Cells and Regenerative Medicine (ISCRM) at the University of Washington.

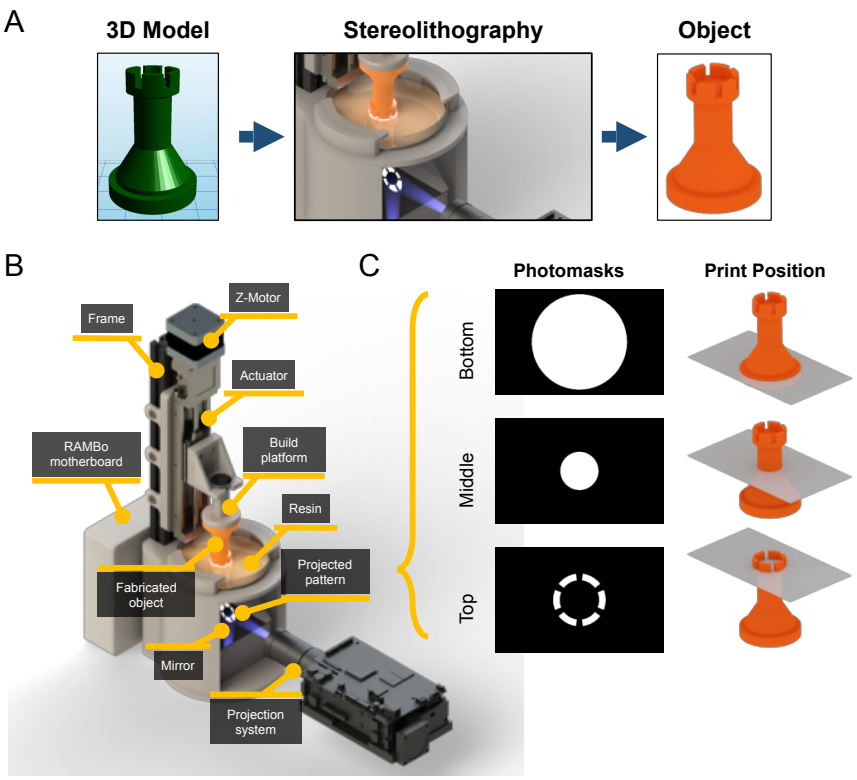

fig. S1: **Stereolithography Apparatus for Tissue Engineering (SLATE). (A)** A schematized workflow for fabrication of 3D objects by projection stereolithography. Photomasks corresponding to a 3D model are projected into a vat containing a photosensitive liquid solution. Upon completion of sequential layer-by-layer photopatterning, a 3D object is obtained. **(B)** 3D rendering of the designed projection stereolithography apparatus. The system consists of a motor, controlled by an actuator, onto which the build platform is attached. The back of the printer houses the RAMBo motherboard which controls the motor and performs input–output with any additional sensors or switches. The front of the printer contains a mirror placed 45° to reflect incident patterns from a projector onto a dish containing the photosensitive materials. All off-white colored parts correspond to parts that were 3D printed out of consumer-grade poly(lactic acid) (PLA) plastic filament. **(C)** Schematic demonstrating photomasks (left) that are generated at different locations along the height of the 3D rook model.

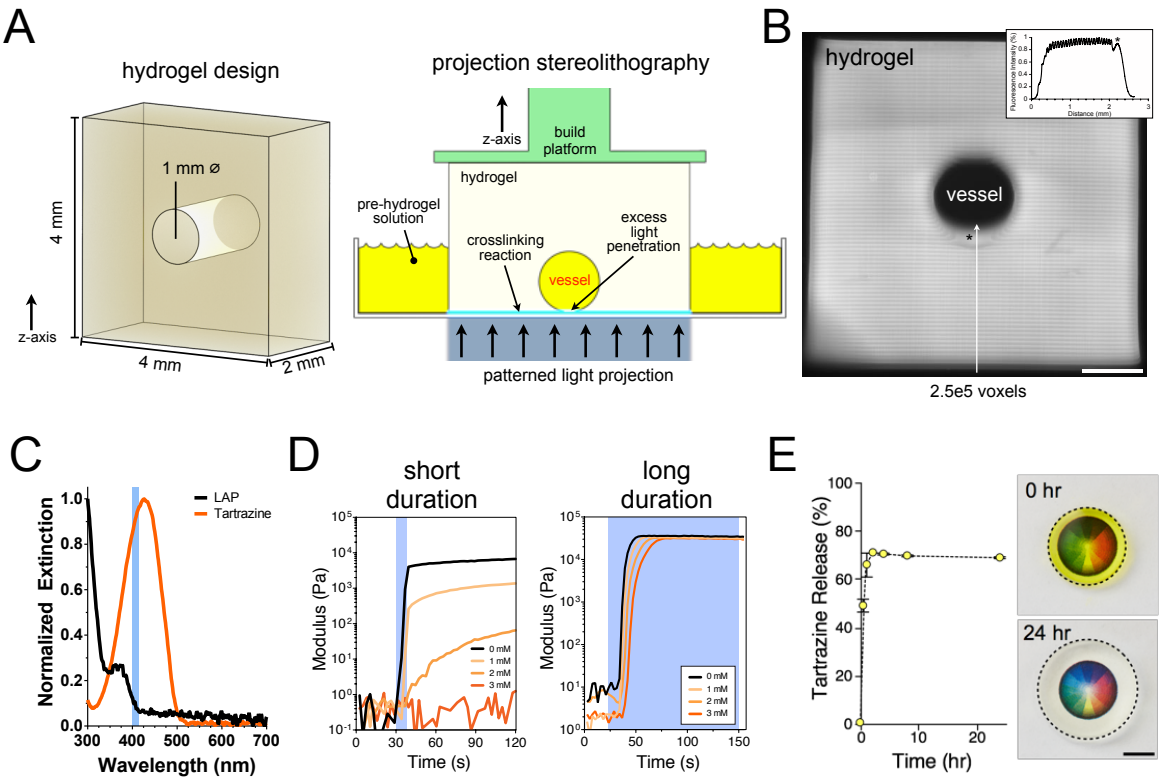

fig. S2: **Fabrication of monolithic hydrogels with patent vessels. (A)** A monolithic hydrogel with a horizontal vessel can be fabricated by projection stereolithography only with suitable photoabsorbers added to the pre-hydrogel solution which can minimize excess light penetration into the nascent vessel (schematized). **(B)** Projection stereolithography with tartrazine yields hydrogels with minimal excess crosslinking in the vessel lumen (asterisk) and shown as line plot inset (bar = 1 mm). **(C)** Absorbance spectra of LAP photoinitiator and photoabsorber tartrazine. The absorbance spectra of tartrazine encompass our light source (vertical bar at 405 nm) which can be used to initiate photocrosslinking via the LAP photoinitiator. **(D)** Photorheology during short duration (left) and long duration (right) light exposures (blue shaded region) demonstrates that tartrazine addition (0-3 mM) slows the induction of crosslinking but does not ultimately interfere with gelation (lines are averaged plots, N = 3). **(E)** Hydrogels release up to 70% tartrazine within hours (exemplified by photos of gels above a color wheel, inset, bar = 5 mm), making fabricated hydrogels suitable for color and fluorescence imaging.

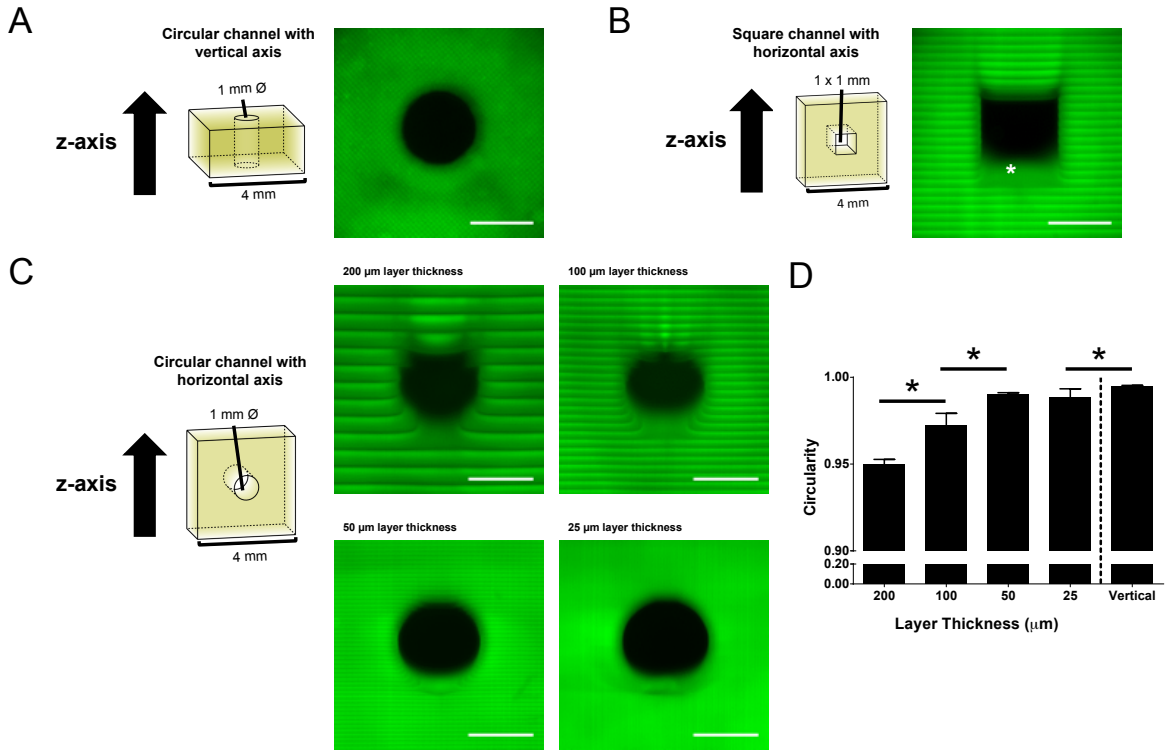

fig. S3: **Fabrication orientation and layer thickness affect fidelity of printed channel.** **(A)** Circular channel of 1 mm diameter fabricated such that the longitudinal axis of the channel is parallel with the print direction. This orientation produces no overhanging features with high circularity (quantified in **(D)**). **(B)** Square channel of 1 mm sides, fabricated in a horizontal orientation perpendicular to the light projection axis. Asterisk denotes region where excess light penetration caused extraneous hydrogel crosslinking. **(C)** Circular channels of 1 mm diameter in a horizontal orientation were printed using a layer thickness of 200, 100, 50, or 25 µm. Note that the 50 µm image is the same image used in **(Fig. 1B)** and is presented again here for completeness. **(D)** Plot of channel circularity (as calculated in **Equation 1**) as a function of layer thickness. Horizontal channel prints are shown left of the dashed line; vertical channel (from **(A)**) is shown at right. As layer height decreases, channels exhibit higher circularity and thus greater geometric fidelity to their original CAD model ($N \geq 3$, asterisk indicates significant difference, $p \leq 0.002$ by Student's t-test, data are shown as mean ± standard deviation). All scale bars = 1 mm.

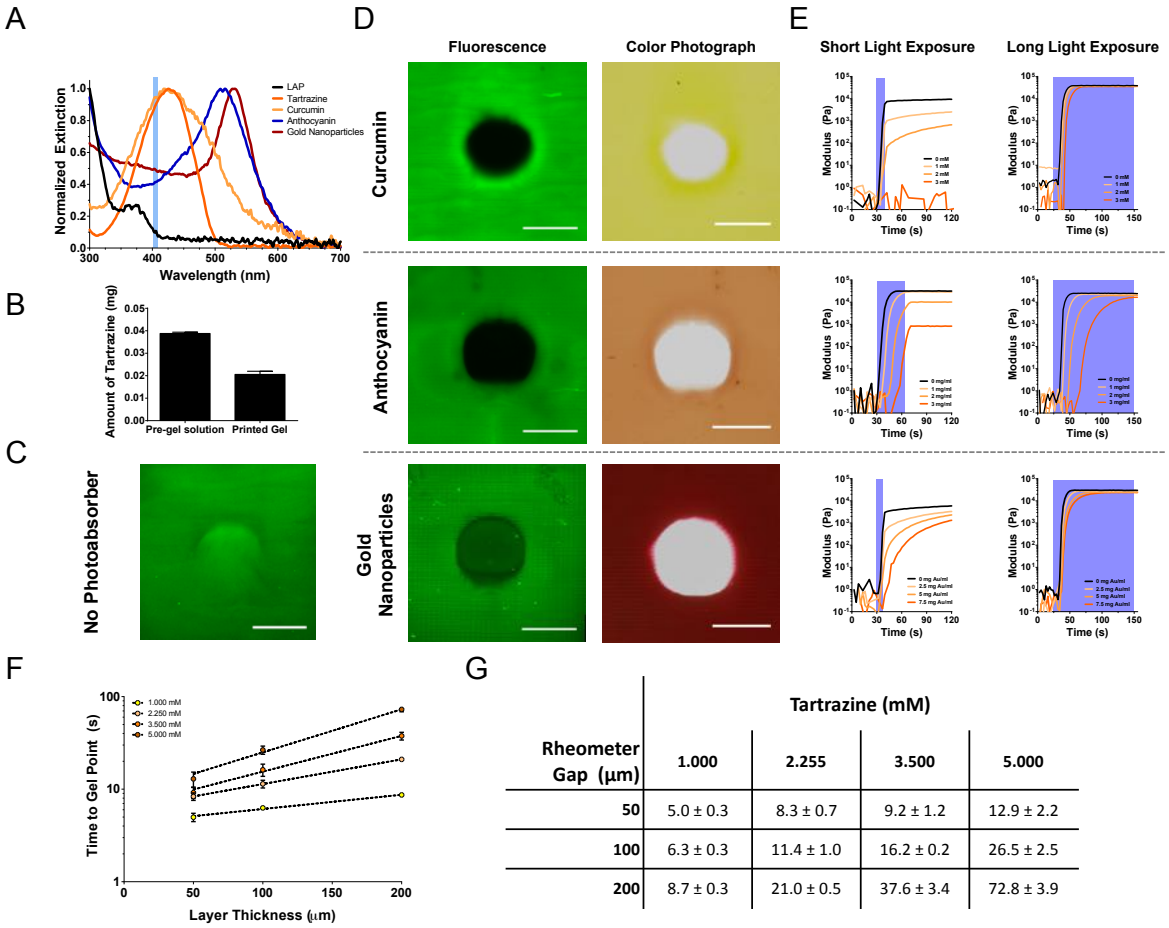

Rheometer Gap (μm)	Tartrazine (mM) 1.000	2.255	3.500	5.000
50	5.0 ± 0.3	8.3 ± 0.7	9.2 ± 1.2	12.9 ± 2.2
100	6.3 ± 0.3	11.4 ± 1.0	16.2 ± 0.2	26.5 ± 2.5
200	8.7 ± 0.3	21.0 ± 0.5	37.6 ± 3.4	72.8 ± 3.9

fig. S4: **Biocompatible photoabsorbers allow fabrication of hydrogels with open channels. (A)** Absorbance spectra of LAP photoinitiator and biocompatible photoabsorbers tartrazine, curcumin, anthocyanin, and 50 nm gold nanoparticles (N = 3). The absorbance spectra of these additives encompass our light source (vertical bar at 405 nm) which can be used to initiate photocrosslinking via the LAP photoinitiator. Note: tartrazine and LAP spectra are replotted from **(fig. S2C)**. **(B)** The amount of tartrazine was found to be lower in a printed gel (4×4×2 mm with 1 mm diameter channel) compared to the starting pre-hydrogel solution (N = 3, data are shown as mean ± standard deviation), which we attribute to its degradation during the radical-mediated photochemical reaction *(45)*. **(C)** Hydrogel, with the horizontal vessel geometry described in **(Fig. 1A)**, fabricated without any photoabsorber additive result in undesired gelation within the vessel, completely occluding it (bar = 1 mm). Rhodamine-dextran was incorporated into the pre-hydrogel mixture to enable fluorescence imaging (colored green here). **(D)** Fluorescence (left) and color photograph (right) images of curcumin (top), anthocyanin (middle), and 50 nm gold nanoparticles (bottom) as photoabsorbers for fabrication of open horizontal channels using stereolithography (bars = 1 mm). FITC-dextran was incorporated into the pre-hydrogel mixture to obtain fluorescence images (colored green here). **(E)** Photorheological studies with short (left) and long (right) duration light exposures with the following additives: curcumin (top), anthocyanin (middle), and 50 nm gold nanoparticles (bottom) (lines are averaged plots, N = 3). **(F)** Working curves for hydrogel formulations of increasing photoabsorber concentration. Each data point represents the time required for a single layer hydrogel of given thickness to reach its gel point during dynamic oscillation and irradiation. **(G)** Table of all data points from **(Fig. S4F)**, data are mean ± standard deviation.

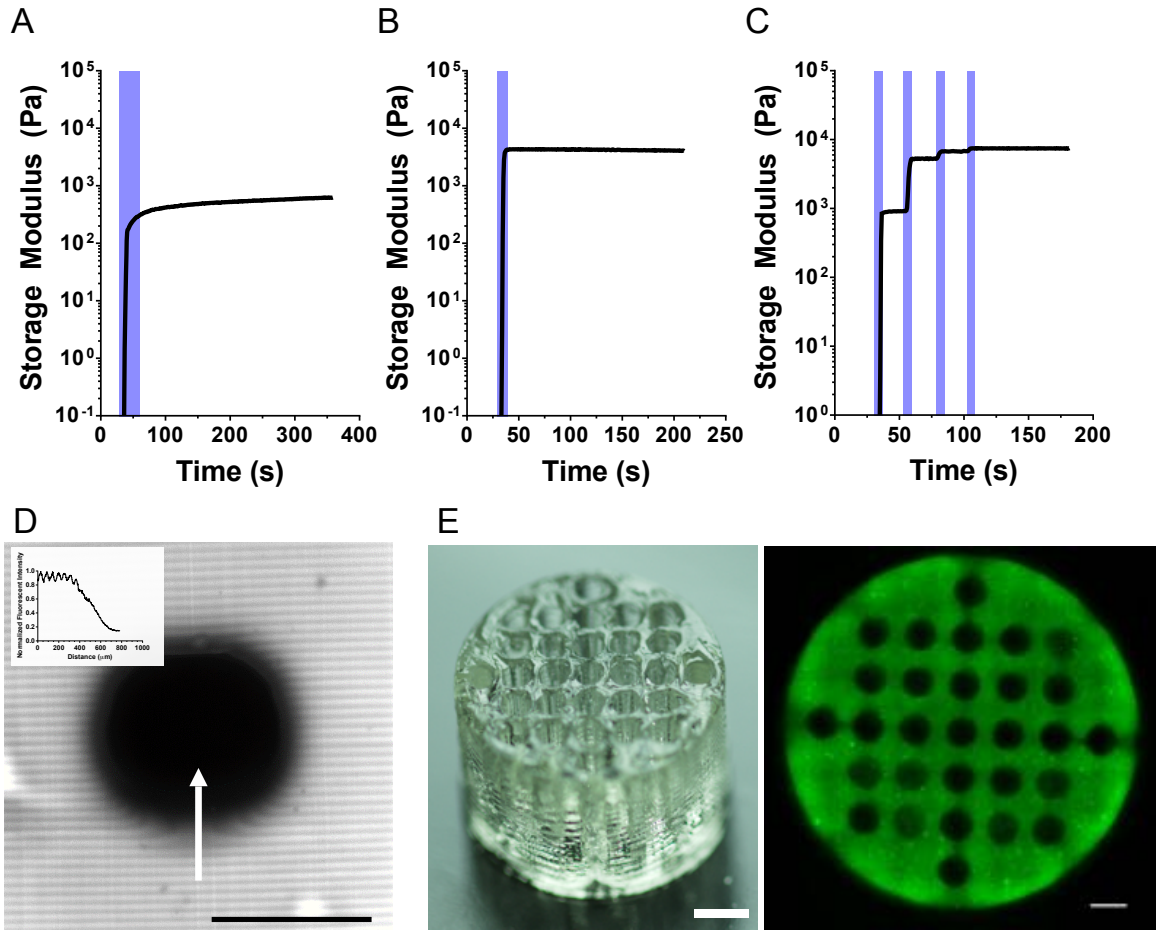

fig. S5: **Compatibility of photoabsorber additives with advanced materials and fabrication strategies.** **(A)** Photorheology of radical-mediated chain-growth photopolymerization with PEGDA and photoabsorber reveals that increases in hydrogel stiffness slowly increase long after light (blue shaded region) is switched off, also known as dark reactions. **(B)** In contrast, with PEG-norbornene and PEG-dithiol step-growth polymerization (thiol-ene click chemistry) in the presence of photoabsorber additives, an increase in hydrogel stiffness stops abruptly after light (shaded blue region) is switched off. **(C)** The staircase-like appearance of step-growth reaction kinetics can be replicated in series with discrete light pulses (shaded blue regions) to yield hydrogels of variable stiffness without the complication of slowly evolving reactions as seen in chain-growth polymerization. **(D)** Projection stereolithography of thiol-ene materials yields hydrogels with minimal excess crosslinking in the vessel lumen and shown as line plot inset (bar = 1 mm). **(E)** Continuous projection stereolithography of hydrogels containing open channels can be achieved (left bar = 2 mm, right bar = 1 mm). FITC-Dextran was incorporated into the pre-hydrogel mixture to obtain fluorescence image (colored green here).

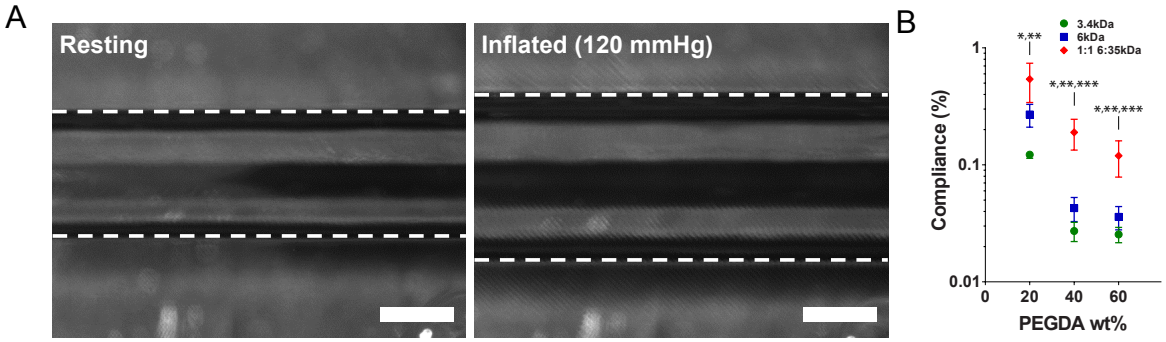

fig. S6: **Compliance measurements of horizontal channels fabricated within hydrogels. (A)** Vessel distension was measured upon application of pneumatic air pressure (hydrogel composition: 20 wt% 6 kDa PEGDA; channel diameter: 1.5 mm; channel length: 20 mm). White dashed lines represent walls of the imaged channel (bar = 1 mm). **(B)** Compliance (as calculated in **Equation 2**) of vessels was found to be dependent on composition of pre-hydrogel solution. Solutions composed of lower polymer molecular weight and higher wt% resulted in hydrogels with lower compliance ($n \geq 4$). Data are shown as mean ± standard deviation, where a single asterisk signifies significance between the 3.4 and 6 kDa, two asterisks signifies significance between 3.4 and 6:35 kDa mixture, and three asterisks signifies significance between 6 and 6:35 kDa mixture (by Student's t-test, $p < 0.05$).

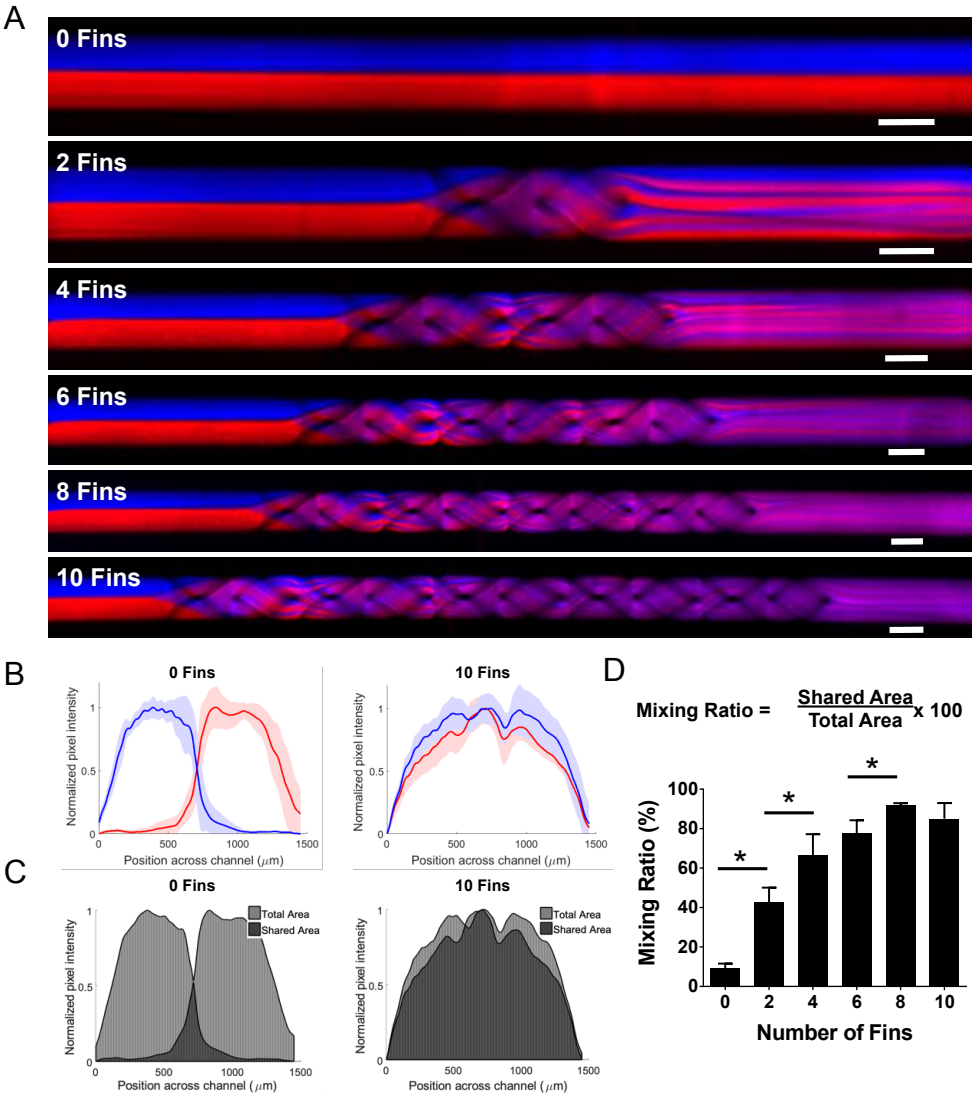

fig. S7: **Quantification of the mixing efficiency of monolithic hydrogels containing perfusable static mixers. (A)** Stitched fluorescence images of printed monolithic hydrogels (80 wt% 6 kDa) containing static mixers with 2 to 10 fin elements and perfused with fluorescent dyes. A printed gel with a channel with 0 fin elements, top, is the negative control. Image of 6 fin static mixer is from **Fig. 1A** and reprinted here for completeness. All scale bars = 1 mm. **(B)** Normalized fluorescence intensity profiles at outlet of a static mixer with 0 or 10 fins, where the bold line represents the average intensity over a 3 mm length of the outlet immediately following the fins and the shaded regions represent standard deviation (N = 3). **(C)** Average intensity data from **(B)** replotted to demonstrate mixing ratio calculations for static mixers. **(D)** Formula for calculating mixing ratio, along with plot showing mean mixing ratio (± standard deviation), where an asterisk signifies significantly more mixing (by Student's t-test, $p < 0.05$) by the group with higher fin number.

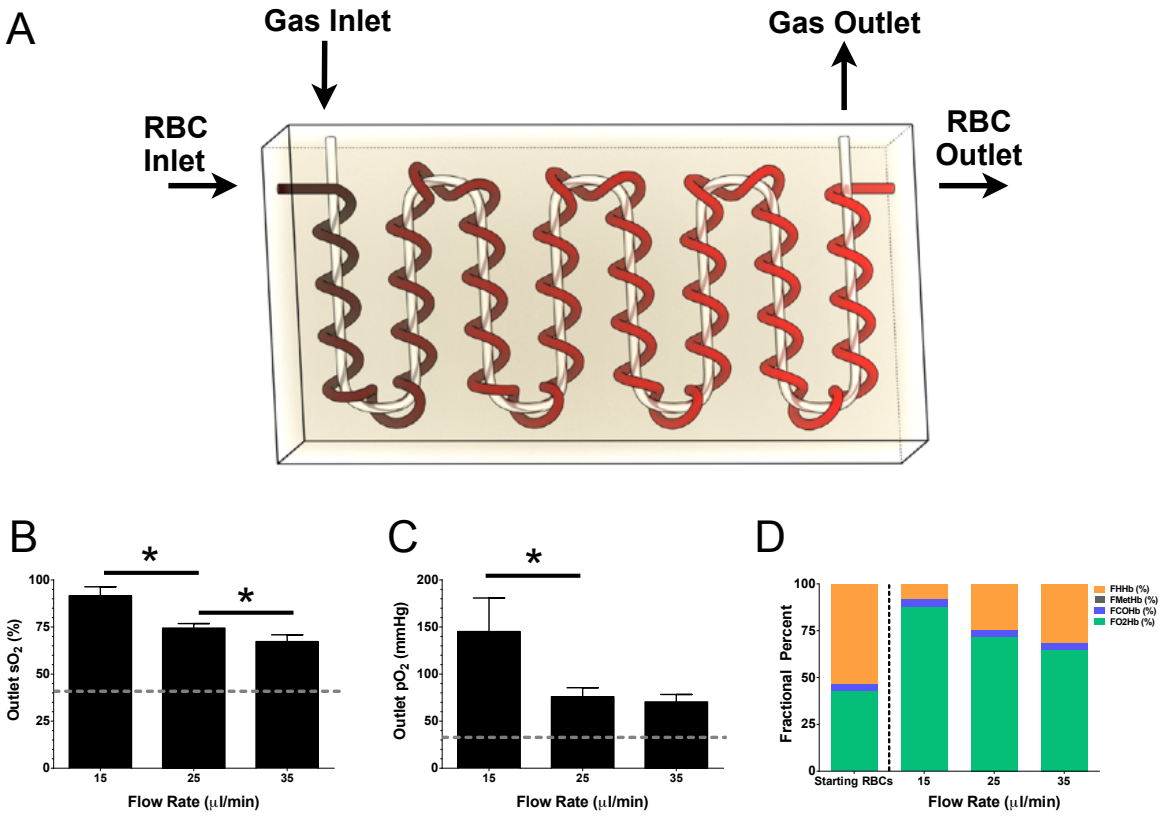

fig. S8: **Oxygenation of perfused human red blood cells in serpentine-helix gels under different flow rates. (A)** Architectural design of a serpentine-helix model used for gas exchange studies here and in **(Fig. 2)**. **(B,C)** Slower perfusion of deoxygenated red blood cells (RBCs) through the vascular network (during gaseous oxygen flow) resulted in higher sO_2 **(B)** and pO_2 **(C)** of the collected RBCs ($N \geq 3$, $p < 2.3e\text{-}4$ by Student's t-test, data are shown as mean ± standard deviation). Dashed gray line indicates the measured sO_2 and pO_2, respectively, of deoxygenated RBCs used for the perfusion. Note that these data include the oxygen perfusion data reported in **Fig. 2G**, reprinted here for completeness. **(D)** The fraction of oxygenated hemoglobin increased significantly with slower flow rates. FHHb = fractional deoxyhemoglobin; FMetHb = fractional methemoglobin; FCOHb = fractional carboxyhemoglobin; FO_2Hb = fractional oxyhemoglobin (data are shown as average of N = 3).

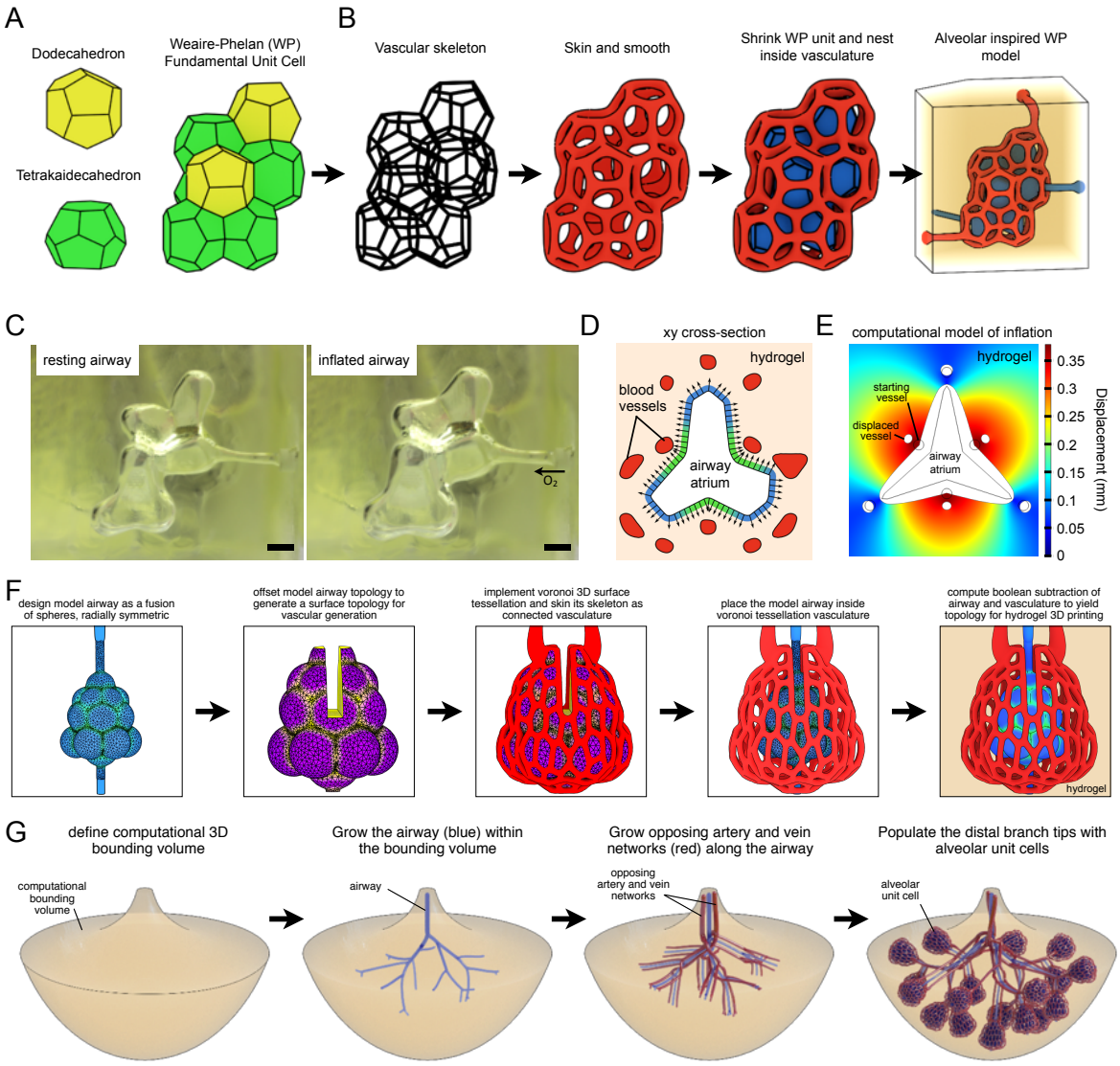

fig. S9: **Design of bioinspired alveoli models.** **(A)** The fundamental Weaire-Phelan (WP) polyhedra *(35)* can be tessellated in 3D to fill space. **(B)** Procedural derivation of the entangled alveolar model from the Weaire-Phelan tessellation. **(C)** Photographs of the printed alveoli model, without RBC flow in the ensheathing vasculature, highlights the airway is smaller at rest (left) compared to the airway during inflation and hydrogel distension (right, 10 kPa, 0.5 Hz) (bars = 1 mm). **(D)** An xy cross-section view of the model with convex (blue) and concave (green) regions of the airway (white), and accompanying blood vessels (red). Normal force arrows converge at concave regions. **(E)** A 2D computational model of a symmetric airway surrounded by circular vessels equidistant from convex or concave regions of the airway (black edges indicate starting positions). Upon airway inflation, concave regions displace and compress adjacent blood vessels. **(F)** To design the distal lung subunit model, the airway was first designed by fusion of spheres with inlet and outlet channels. Then, the airway topology was offset and used as a template for vascular generation by implementing a voronoi 3D surface tesselation, skeletonization, and skinning. Finally, a boolean subtraction of these two topologies from a solid volume was performed which represents the final hydrogel design. **(G)** A path towards generation of lung-mimetic model by populating branch tips of airway and offset vascular networks, grown within a defined computational 3D bounding volume, with the distal lung subunit model.

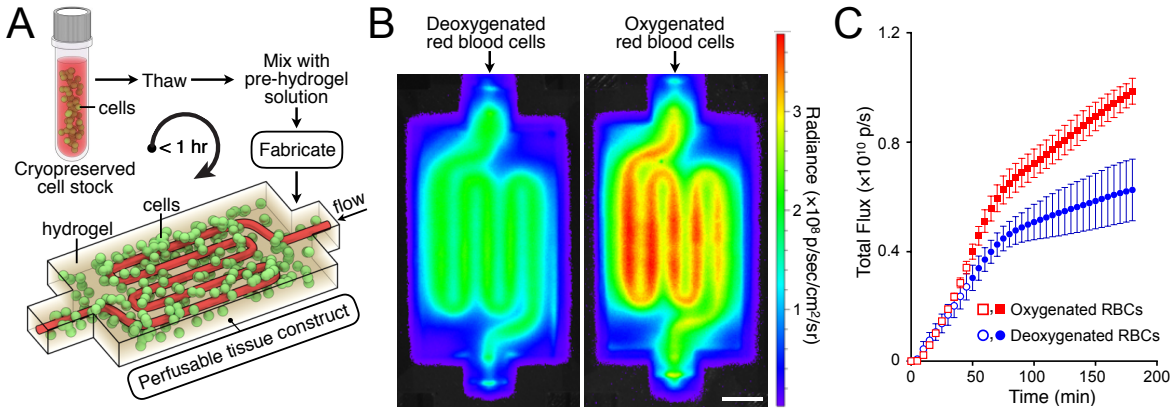

fig. S10: **Rapid biomanufacturing with cryopreserved cell stocks and non-invasive characterization of cellular activity.** **(A)** Cryopreserved cell stocks are thawed and immediately used in projection stereolithography to yield perfusable tissues with patterned vessel architectures. The total procedure from cell thaw to perfusion experiments takes less than 1 hr. **(B)** Using this workflow, fabricated tissue constructs containing mammalian cells (2.5×10^7 cells/mL) expressing firefly luciferase (Luc2P) were perfused with deoxygenated or oxygenated RBCs along with luciferin substrate. Luminescence quantification (t = 3 hr) demonstrates increased light emission from cells within gels perfused with oxygenated RBCs (bar = 5 mm). **(C)** Full 3 hr time course of perfusion experiment from **(B)** plotted as total light flux emitted from cells within hydrogels. Error bars indicate standard deviation. Filled symbols indicate a statistically significant difference between groups at each time point (N = 3, $p < 0.04$ by Student's t-test, data are shown as mean ± standard deviation).

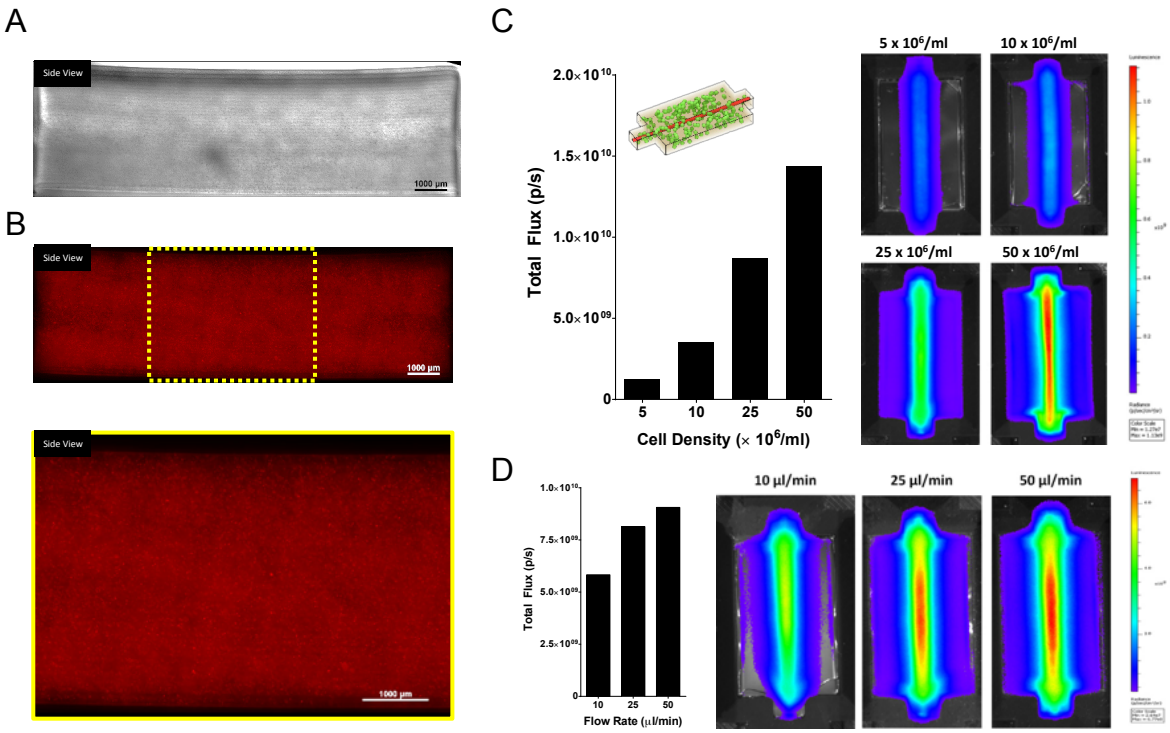

fig. S11: **Cell encapsulation shows uniform cell distribution and enables luminescent screening. (A,B)** Incorporation of xanthan gum into the pre-hydrogel solution resulted in homogeneous distribution of cells along the height of the gel as seen in the phase **(A)** and fluorescence images **(B)** of a side view (xz plane) of a fabricated 20 wt% hydrogel containing HEK mCherry cells (20×10^6 cells/mL) (bars = 1 mm). **(C, D)** Total light output of HEK Luc2P cells encapsulated in PEGDA hydrogels containing a horizontal 0.8 mm diameter channel at different cell densities **(C)** and different flow rates of luciferin substrate **(D)**.

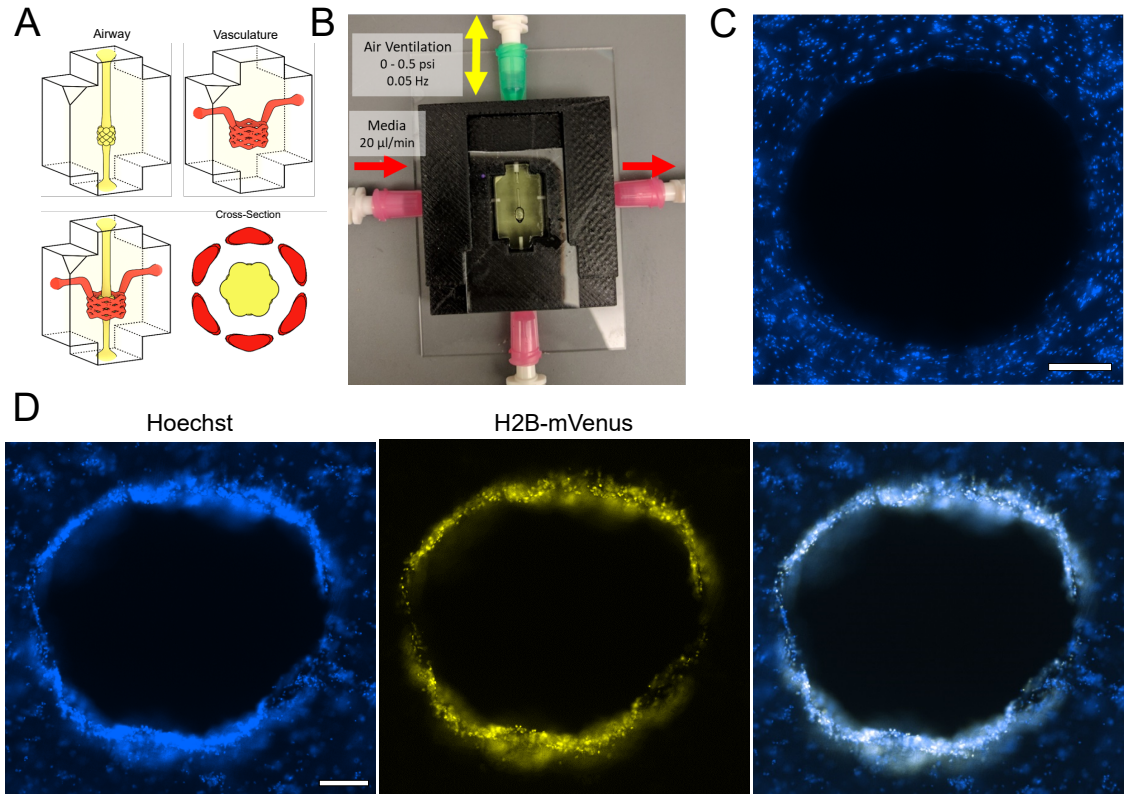

fig. S12: **Monolithic lung-mimetic perfusion and ventilation tissue culture system.** **(A)** Bioinspired design of an alveolar sac with surrounding pulmonary vasculature. Overall size of model is 9×11.8×4.3 mm (x,y,z) with smallest channel diameter of 400 µm and alveolus diameter of 600 µm. **(B)** Photo of the fluidic connections to the printed gel for perfusion through the vascular channel and ventilation of the airway vessel. **(C)** Hydrogels were fabricated with IMR-90 fibroblasts (10×10^6 cells/mL) encapsulated in the bulk of the hydrogel, including the interstitial region. Ventilation of the airway under perfusion tissue culture through the vasculature (20 µL/min over 5 days) maintained patency of the airway as seen in cross-sectional imaging after staining for nuclei (Hoechst). Scale bar = 250 µm. **(D)** Seeded A549 epithelial-like cells (expressing H2B-mVenus, center) are attached to the airway lumen of printed hydrogels containing encapsulated fibroblasts in the interstitial zone. Scale bar = 500 µm.

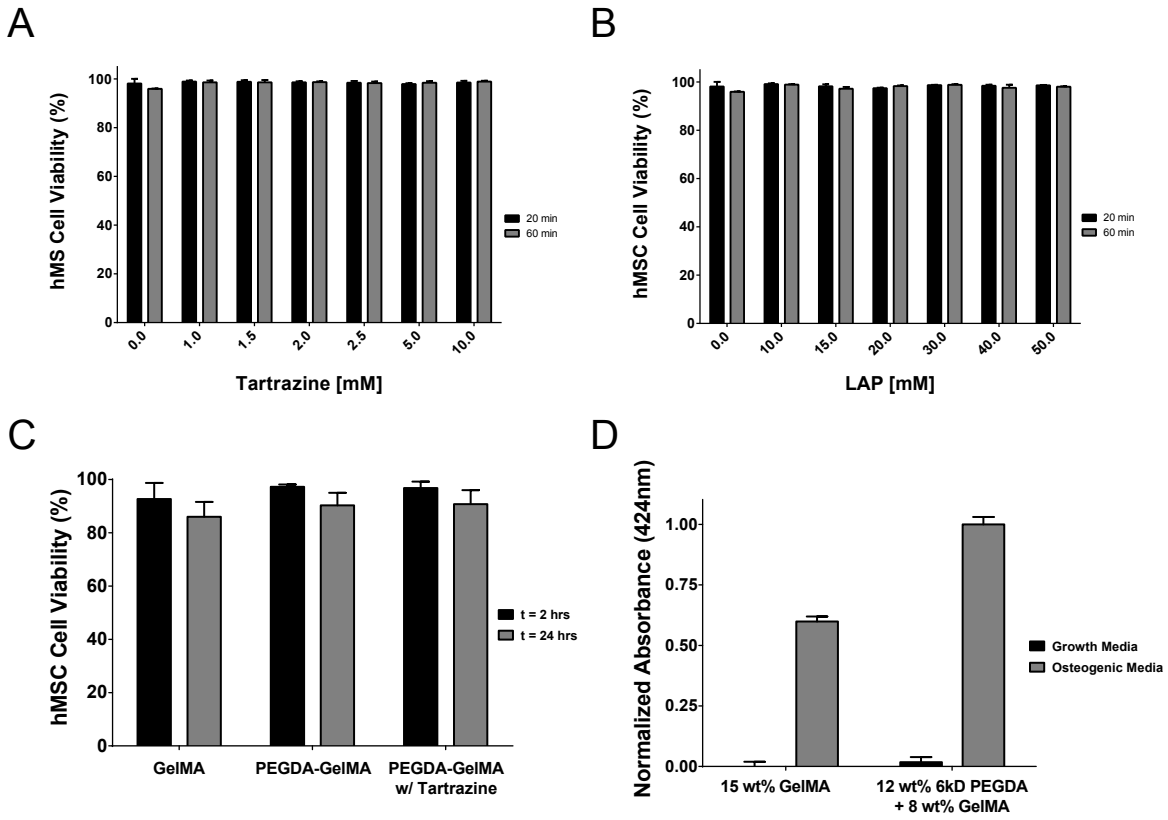

fig. S13: **Inclusion of tartrazine does not affect viability and differentiation of human mesenchymal stem cells. (A,B)** Human mesenchymal stem cells (hMSCs) incubated with 1-10 mM tartrazine **(A)** and 10-50 mM LAP **(B)** for 20 and 60 min resulted in high cell viability ($N \geq 2$). Note: data for 0.0 mM tartrazine and 0.0 mM LAP are the identical positive control data set since these studies were run concurrently. **(C)** hMSCs fabricated in cylindrical hydrogels demonstrated high cell viability in bioactive hydrogels ($N = 3$, data are shown as mean ± standard deviation). **(D)** Quantification of osteogenic differentiation of hMSCs encapsulated in hydrogels fabricated with tartrazine ($N = 3$, data are shown as mean ± standard deviation).

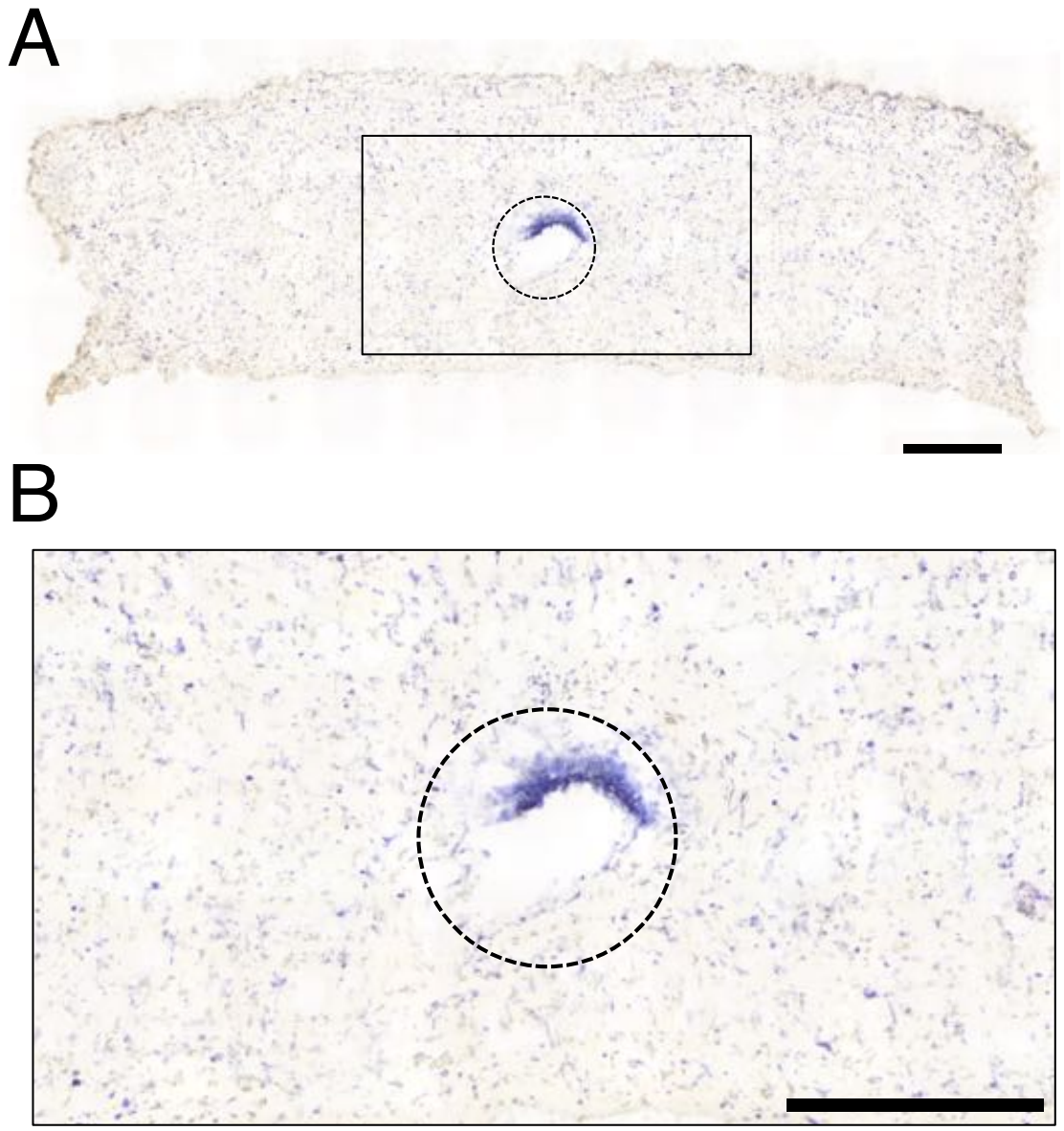

fig. S14: **hMSC differentiation of perfused single channel gels. (A)** Alkaline phosphatase (ALP) staining of hMSC tissue cross-section from a hydrogel that underwent osteogenic media perfusion for 14 days, vascular channel is highlighted with the dotted circle. ALP stained was found strongly along the perimeter of the perfused channel with some positive staining throughout the bulk of the gel. **(B)** Close-up of boxed section from **(A)** near the perfused channel. Scale bars = 1 mm.

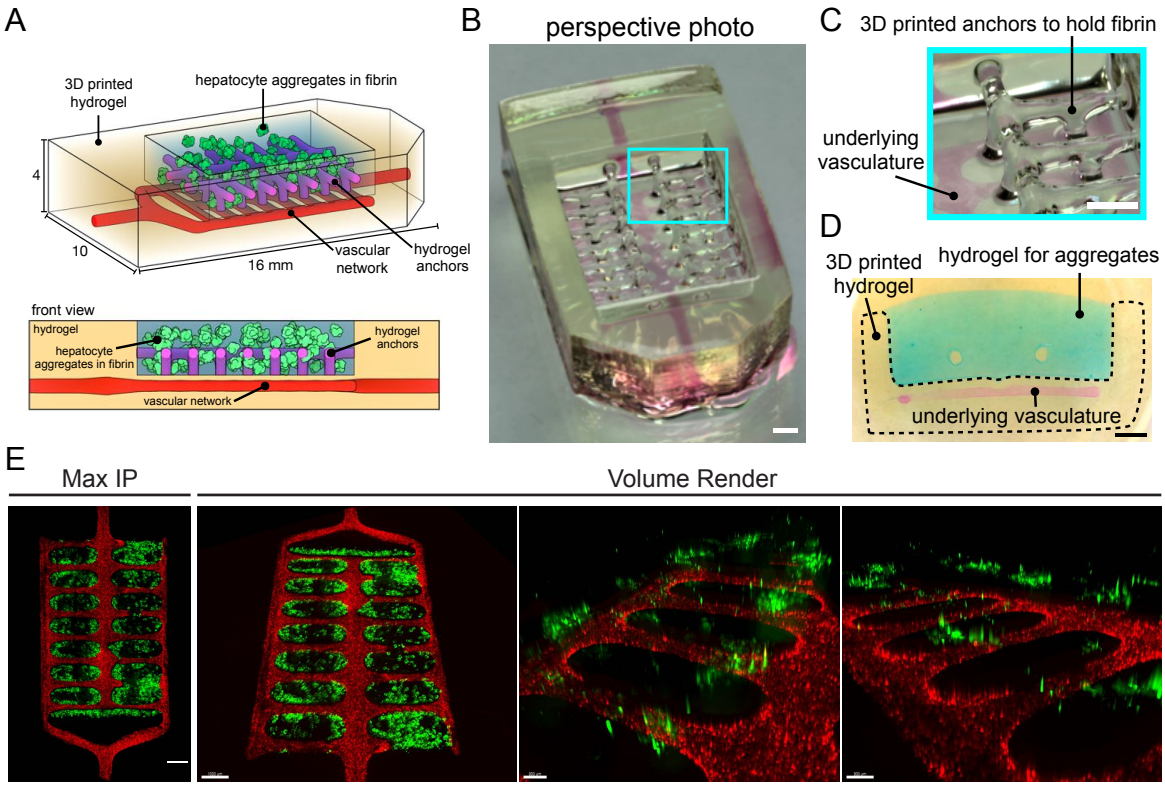

fig. S15: **Additional imaging and development of hepatic hydrogel carriers. (A)** 3D printed hydrogel carriers accommodate primary hepatocyte aggregates **(green)** suspended in fibrin **(blue)**, entangled with hydrogel anchors **(purple)** and has an underlying patterned vascular network (**red**). **(B)** 3D printed chamber demonstrate perfusable vasculature (red), and hydrogel anchors (bar = 1 mm). **(C)** Magnified view of highlighted region from **(B)** showing hydrogel anchors and underlying perfusable vasculature **(red)** (bar = 1 mm). **(D)** a 250 μm cross-section view demonstrates the fibrin seeding volume **(blue)** and underlying vasculature **(red)** (bar = 1 mm). **(E)** Confocal maximum intensity projection (Max IP, left) and volumetric rendering of endothelial cords (red) and hepatocytes (green). These data supplement main text **Fig. 4E)** (left two images bar = 1 mm, right two images bar = 300 μm).

Movie S1: **Movie compilation to help explain the functional intravascular bicuspid valve design and performance.** We first illustrate the design of the bicuspid valve, followed by phase contrast imaging and fluorescence imaging videos of anterograde and retrograde flow of fluorescent beads. The valve is open under anterograde flow and closes under retrograde flow. Note also the mirror image vortices in the sinus region during anterograde flows. This movie supplements **Fig. 1**.

Movie S2: **Movie compilation of fabricated hydrogels with entangled vascular networks.** This movie supplements **Fig. 2**. Perfusion video of red dye injected into helical channel wrapped around axial vessel filled with blue dye. Rotational video of 1°, 2° Hilbert Curve filled with different colored dyes into individual channels. Animation of layers used for stereolithographic fabrication of torus model, followed by perfusion of red dye through the (3,10) torus knot. Filling of the channels in the torus model with colored dyes enabled μCT acquisition, reconstruction, and visualization of perfusable channels.

Movie S3: **Movie compilation illustrating the design and function of the bioinspired alveolar model based on the Weaire-Phelan foam topology.** Cyclic ventilation of the airway during RBC perfusion through ensheathing vasculature demonstrates valving of the vasculature by nearby concave airway regions. This movie supplements **Fig. 3**.

Movie S4: **Movie compilation illustrating the design and function of the scalable voronoi lung-mimetic model.** We show an animation explaining the generative lung topology algorithm where an airway is grown, inlet and outlet vasculature track the airway on opposing sides, and the tips of all branches are then populated with the distal lung subunit. Movie footage of ventilation and perfusion experiments are shown of the distal lung subunit as well as color-filtered views of bidirectional blood flow observed during ventilation and perfusion. This movie supplements **Fig. 3**.

Movie S5: **Luminescence imaging of fabricated tissue constructs perfused with media containing luciferin substrate and either deoxygenated or oxygenated RBCs.** Luminescence of entrapped Luc2P-expressing HEK cells is boosted in tissues perfused with oxygenated RBCs. Images from complete time course shown in **fig. S10**.

References and Notes

1. R. Monahan-Earley, A. M. Dvorak, W. C. Aird, Evolutionary origins of the blood vascular system and endothelium. *J. Thromb. Haemost.* **11** (suppl. 1), 46–66 (2013). doi:10.1111/jth.12253 Medline

2. G. R. Scott, Elevated performance: The unique physiology of birds that fly at high altitudes. *J. Exp. Biol.* **214**, 2455–2462 (2011). doi:10.1242/jeb.052548 Medline

3. E. R. Schachner, J. R. Hutchinson, C. Farmer, Pulmonary anatomy in the Nile crocodile and the evolution of unidirectional airflow in Archosauria. *PeerJ* **1**, e60 (2013). doi:10.7717/peerj.60 Medline

4. C. G. Farmer, The Evolution of Unidirectional Pulmonary Airflow. *Physiology* **30**, 260–272 (2015). doi:10.1152/physiol.00056.2014 Medline

5. Supplementary figures, as well as materials and methods, are available as supplementary materials.

6. J. R. Tumbleston, D. Shirvanyants, N. Ermoshkin, R. Janusziewicz, A. R. Johnson, D. Kelly, K. Chen, R. Pinschmidt, J. P. Rolland, A. Ermoshkin, E. T. Samulski, J. M. DeSimone, Additive manufacturing. Continuous liquid interface production of 3D objects. *Science* **347**, 1349–1352 (2015). doi:10.1126/science.aaa2397 Medline

7. B. E. Kelly, I. Bhattacharya, H. Heidari, M. Shusteff, C. M. Spadaccini, H. K. Taylor, Volumetric additive manufacturing via tomographic reconstruction. *Science* **363**, 1075–1079 (2019). doi:10.1126/science.aau7114 Medline

8. J. S. Miller, K. R. Stevens, M. T. Yang, B. M. Baker, D.-H. T. Nguyen, D. M. Cohen, E. Toro, A. A. Chen, P. A. Galie, X. Yu, R. Chaturvedi, S. N. Bhatia, C. S. Chen, Rapid casting of patterned vascular networks for perfusable engineered three-dimensional tissues. *Nat. Mater.* **11**, 768–774 (2012). doi:10.1038/nmat3357 Medline

9. T. J. Hinton, Q. Jallerat, R. N. Palchesko, J. H. Park, M. S. Grodzicki, H.-J. Shue, M. H. Ramadan, A. R. Hudson, A. W. Feinberg, Three-dimensional printing of complex biological structures by freeform reversible embedding of suspended hydrogels. *Sci. Adv.* **1**, e1500758 (2015). doi:10.1126/sciadv.1500758 Medline

10. T. Bhattacharjee, S. M. Zehnder, K. G. Rowe, S. Jain, R. M. Nixon, W. G. Sawyer, T. E. Angelini, Writing in the granular gel medium. *Sci. Adv.* **1**, e1500655 (2015). doi:10.1126/sciadv.1500655 Medline

11. D. B. Kolesky, K. A. Homan, M. A. Skylar-Scott, J. A. Lewis, Three-dimensional bioprinting of thick vascularized tissues. *Proc. Natl. Acad. Sci. U.S.A.* **113**, 3179–3184 (2016). doi:10.1073/pnas.1521342113 Medline

12. H.-W. Kang, S. J. Lee, I. K. Ko, C. Kengla, J. J. Yoo, A. Atala, A 3D bioprinting system to produce human-scale tissue constructs with structural integrity. *Nat. Biotechnol.* **34**, 312–319 (2016). doi:10.1038/nbt.3413 Medline

13. V. Liu Tsang, A. A. Chen, L. M. Cho, K. D. Jadin, R. L. Sah, S. DeLong, J. L. West, S. N. Bhatia, Fabrication of 3D hepatic tissues by additive photopatterning of cellular hydrogels. *FASEB J.* **21**, 790–801 (2007). doi:10.1096/fj.06-7117com Medline

14. H. Lin, D. Zhang, P. G. Alexander, G. Yang, J. Tan, A. W.-M. Cheng, R. S. Tuan, Application of visible light-based projection stereolithography for live cell-scaffold fabrication with designed architecture. *Biomaterials* **34**, 331–339 (2013). doi:10.1016/j.biomaterials.2012.09.048 Medline

15. J. A. S. Neiman, R. Raman, V. Chan, M. G. Rhoads, M. S. B. Raredon, J. J. Velazquez, R. L. Dyer, R. Bashir, P. T. Hammond, L. G. Griffith, Photopatterning of hydrogel scaffolds coupled to filter materials using stereolithography for perfused 3D culture of hepatocytes. *Biotechnol. Bioeng.* **112**, 777–787 (2015). doi:10.1002/bit.25494 Medline

16. X. Ma, X. Qu, W. Zhu, Y.-S. Li, S. Yuan, H. Zhang, J. Liu, P. Wang, C. S. E. Lai, F. Zanella, G.-S. Feng, F. Sheikh, S. Chien, S. Chen, Deterministically patterned biomimetic human iPSC-derived hepatic model via rapid 3D bioprinting. *Proc. Natl. Acad. Sci. U.S.A.* **113**, 2206–2211 (2016). doi:10.1073/pnas.1524510113 Medline

17. M. S. Hahn, J. S. Miller, J. L. West, Three-Dimensional Biochemical and Biomechanical Patterning of Hydrogels for Guiding Cell Behavior. *Adv. Mater.* **18**, 2679–2684 (2006). doi:10.1002/adma.200600647

18. C. A. DeForest, K. S. Anseth, Cytocompatible click-based hydrogels with dynamically tunable properties through orthogonal photoconjugation and photocleavage reactions. *Nat. Chem.* **3**, 925–931 (2011). doi:10.1038/nchem.1174 Medline

19. K. A. Heintz, M. E. Bregenzer, J. L. Mantle, K. H. Lee, J. L. West, J. H. Slater, Fabrication of 3D Biomimetic Microfluidic Networks in Hydrogels. *Adv. Healthc. Mater.* **5**, 2153–2160 (2016). doi:10.1002/adhm.201600351 Medline

20. T. M. Fonovich, Sudan dyes: Are they dangerous for human health? *Drug Chem. Toxicol.* **36**, 343–352 (2013). doi:10.3109/01480545.2012.710626 Medline

21. S. Kumar, J. Aaron, K. Sokolov, Directional conjugation of antibodies to nanoparticles for synthesis of multiplexed optical contrast agents with both delivery and targeting moieties. *Nat. Protoc.* **3**, 314–320 (2008). doi:10.1038/nprot.2008.1 Medline

22. L. J. Stevens, J. R. Burgess, M. A. Stochelski, T. Kuczek, Amounts of artificial food dyes and added sugars in foods and sweets commonly consumed by children. *Clin. Pediatr.* **54**, 309–321 (2015). doi:10.1177/0009922814530803 Medline

23. M. Li, W. He, Y. Liu, H. Wu, W. G. Wamer, Y. M. Lo, J.-J. Yin, FD&C Yellow No. 5 (tartrazine) degradation via reactive oxygen species triggered by TiO_2 and Au/TiO_2 nanoparticles exposed to simulated sunlight. *J. Agric. Food Chem.* **62**, 12052–12060 (2014). doi:10.1021/jf5045052 Medline

24. C. A. DeForest, B. D. Polizzotti, K. S. Anseth, Sequential click reactions for synthesizing and patterning three-dimensional cell microenvironments. *Nat. Mater.* **8**, 659–664 (2009). doi:10.1038/nmat2473 Medline

25. A. D. Stroock, S. K. Dertinger, A. Ajdari, I. Mezic, H. A. Stone, G. M. Whitesides, Chaotic mixer for microchannels. *Science* **295**, 647–651 (2002). doi:10.1126/science.1066238 Medline

26. D. Therriault, S. R. White, J. A. Lewis, Chaotic mixing in three-dimensional microvascular networks fabricated by direct-write assembly. *Nat. Mater.* **2**, 265–271 (2003). doi:10.1038/nmat863 Medline

27. A. Ghanem, T. Lemenand, D. Della Valle, H. Peerhossaini, Static mixers: Mechanisms, applications, and characterization methods – A review. *Chem. Eng. Res. Des.* **92**, 205–228 (2014). doi:10.1016/j.cherd.2013.07.013

28. F. Lurie, R. L. Kistner, B. Eklof, D. Kessler, Mechanism of venous valve closure and role of the valve in circulation: A new concept. *J. Vasc. Surg.* **38**, 955–961 (2003). doi:10.1016/S0741-5214(03)00711-0 Medline

29. E. Bazigou, T. Mäkinen, Flow control in our vessels: Vascular valves make sure there is no way back. *Cell. Mol. Life Sci.* **70**, 1055–1066 (2013). doi:10.1007/s00018-012-1110-6 Medline

30. C. C. W. Hsia, D. M. Hyde, E. R. Weibel, Lung Structure and the Intrinsic Challenges of Gas Exchange. *Compr. Physiol.* **6**, 827–895 (2016). doi:10.1002/cphy.c150028 Medline

31. J. Mead, T. Takishima, D. Leith, Stress distribution in lungs: A model of pulmonary elasticity. *J. Appl. Physiol.* **28**, 596–608 (1970). doi:10.1152/jappl.1970.28.5.596 Medline

32. A. Linhartová, W. Caldwell, A. E. Anderson, A proposed alveolar model for adult human lungs: The regular dodecahedron. *Anat. Rec.* **214**, 266–272 (1986). doi:10.1002/ar.1092140305 Medline

33. Y. C. Fung, A model of the lung structure and its validation. *J. Appl. Physiol.* **64**, 2132–2141 (1988). doi:10.1152/jappl.1988.64.5.2132 Medline

34. P. Hofemeier, J. Sznitman, Role of alveolar topology on acinar flows and convective mixing. *J. Biomech. Eng.* **136**, 061007 (2014). doi:10.1115/1.4027328 Medline

35. D. Weaire, R. Phelan, A counter-example to Kelvin's conjecture on minimal surfaces. *Philos. Mag. Lett.* **69**, 107–110 (1994). doi:10.1080/09500839408241577

36. J. B. West, C. T. Dollery, A. Naimark, Distribution of blood flow in isolated lung; relation to vascular and alveolar pressures. *J. Appl. Physiol.* **19**, 713–724 (1964). doi:10.1152/jappl.1964.19.4.713 Medline

37. D. Huh, B. D. Matthews, A. Mammoto, M. Montoya-Zavala, H. Y. Hsin, D. E. Ingber, Reconstituting organ-level lung functions on a chip. *Science* **328**, 1662–1668 (2010). doi:10.1126/science.1188302 Medline

38. K. R. Stevens, M. A. Scull, V. Ramanan, C. L. Fortin, R. R. Chaturvedi, K. A. Knouse, J. W. Xiao, C. Fung, T. Mirabella, A. X. Chen, M. G. McCue, M. T. Yang, H. E. Fleming, K. Chung, Y. P. de Jong, C. S. Chen, C. M. Rice, S. N. Bhatia, In situ expansion of engineered human liver tissue in a mouse model of chronic liver disease. *Sci. Transl. Med.* **9**, eaah5505 (2017). doi:10.1126/scitranslmed.aah5505 Medline

39. J. S. Miller, Dataset for: Multivascular networks and functional intravascular topologies within biocompatible hydrogels, Version 1.0, Zenodo (2019); https://doi.org/10.5281/zenodo.2614071.

40. A. P. Randles, V. Kale, J. Hammond, W. Gropp, E. Kaxiras, “Performance analysis of the lattice Boltzmann model beyond Navier-Stokes” in *Proceedings of the 2013 IEEE 27th International Symposium on Parallel and Distributed Processing* (IEEE, 2013), pp. 1063–1074.

41. L. Andrus, S. Marukian, C. T. Jones, M. T. Catanese, T. P. Sheahan, J. W. Schoggins, W. T. Barry, L. B. Dustin, K. Trehan, A. Ploss, S. N. Bhatia, C. M. Rice, Expression of paramyxovirus V proteins promotes replication and spread of hepatitis C virus in cultures of primary human fetal liver cells. *Hepatology* **54**, 1901–1912 (2011). doi:10.1002/hep.24557 Medline

42. J. S. Miller, C. J. Shen, W. R. Legant, J. D. Baranski, B. L. Blakely, C. S. Chen, Bioactive hydrogels made from step-growth derived PEG-peptide macromers. *Biomaterials* **31**, 3736–3743 (2010). doi:10.1016/j.biomaterials.2010.01.058 Medline

43. B. D. Fairbanks, M. P. Schwartz, C. N. Bowman, K. S. Anseth, Photoinitiated polymerization of PEG-diacrylate with lithium phenyl-2,4,6-trimethylbenzoylphosphinate: Polymerization rate and cytocompatibility. *Biomaterials* **30**, 6702–6707 (2009). doi:10.1016/j.biomaterials.2009.08.055 Medline

44. H. Shirahama, B. H. Lee, L. P. Tan, N.-J. Cho, Precise Tuning of Facile One-Pot Gelatin Methacryloyl (GelMA) Synthesis. *Sci. Rep.* **6**, 31036 (2016). doi:10.1038/srep31036 Medline

45. P. Oancea, V. Meltzer, Kinetics of tartrazine photodegradation by UV/H2O2 in aqueous solution. *Chem. Pap.* **68**, 105 (2014). doi:10.2478/s11696-013-0426-5

46. N. L’Heureux, N. Dusserre, G. Konig, B. Victor, P. Keire, T. N. Wight, N. A. F. Chronos, A. E. Kyles, C. R. Gregory, G. Hoyt, R. C. Robbins, T. N. McAllister, Human tissue-engineered blood vessels for adult arterial revascularization. *Nat. Med.* **12**, 361–365 (2006). doi:10.1038/nm1364 Medline

47. C. D. Armeniades, W. C. Johnson, R. Thomas, “Mixing device,” U.S. Patent 3,286,992 (1966).

48. M. F. Coakley, D. E. Hurt, N. Weber, M. Mtingwa, E. C. Fincher, V. Alekseyev, D. T. Chen, A. Yun, M. Gizaw, J. Swan, T. S. Yoo, Y. Huyen, The NIH 3D Print Exchange: A Public Resource for Bioscientific and Biomedical 3D Prints. *3D Print. Addit. Manuf.* **1**, 137–140 (2014). doi:10.1089/3dp.2014.1503 Medline

49. K.-H. Nam, E. Yeom, H. Ha, S.-J. Lee, Velocity field measurements of valvular blood flow in a human superficial vein using high-frequency ultrasound speckle image velocimetry. *Int. J. Cardiovasc. Imaging* **28**, 69–77 (2012). doi:10.1007/s10554-010-9778-x Medline

50. R. Theunissen, F. Scarano, M. L. Riethmuller, An adaptive sampling and windowing interrogation method in PIV. *Meas. Sci. Technol.* **18**, 275–287 (2006). doi:10.1088/0957-0233/18/1/034

51. J. B. Segur, “Physical properties of glycerine and its solutions” (Glycerine Producers’ Association, 1963).

52. A. V. Brikov, A. N. Markin, S. V. Sukhoverkhov, V. A. Avramenko, Rheological properties of poly(ethylene glycol) solutions and gels. *Dokl. Phys. Chem.* **469**, 121–123 (2016). doi:10.1134/S0012501616080030

53. S. Chen, G. D. Doolen, Lattice boltzmann method for fluid flows. *Annu. Rev. Fluid Mech.* **30**, 329–364 (1998). doi:10.1146/annurev.fluid.30.1.329

54. Y. Kim, S. Lim, S. V. Raman, O. P. Simonetti, A. Friedman, Blood flow in a compliant vessel by the immersed boundary method. *Ann. Biomed. Eng.* **37**, 927–942 (2009). doi:10.1007/s10439-009-9669-2 Medline

55. J. Gounley, E. W. Draeger, A. Randles, Numerical simulation of a compound capsule in a constricted microchannel. *Procedia Comput. Sci.* **108**, 175–184 (2017). doi:10.1016/j.procs.2017.05.209 Medline

56. C. S. Peskin, The immersed boundary method. *Acta Numer.* **11**, 479 (2002). doi:10.1017/S0962492902000077

57. C. S. Peskin, Flow patterns around heart valves: A numerical method. *J. Comput. Phys.* **10**, 252–271 (1972). doi:10.1016/0021-9991(72)90065-4

58. B. E. Griffith, X. Luo, D. M. McQueen, C. S. Peskin, Simulating the fluid dynamics of natural and prosthetic heart valves using the immersed boundary method. *Int. J. Appl. Mech.* **01**, 137–177 (2009). doi:10.1142/S1758825109000113

59. J. P. Freyer, D. Fillak, J. H. Jett, Use of xantham gum to suspend large particles during flow cytometric analysis and sorting. *Cytometry* **10**, 803–806 (1989). doi:10.1002/cyto.990100620 Medline

60. E. H. Moriyama, M. J. Niedre, M. T. Jarvi, J. D. Mocanu, Y. Moriyama, P. Subarsky, B. Li, L. D. Lilge, B. C. Wilson, The influence of hypoxia on bioluminescence in luciferase-transfected gliosarcoma tumor cells in vitro. *Photochem. Photobiol. Sci.* **7**, 675–680 (2008). doi:10.1039/b719231b Medline

61. S. Pedron, B. A. C. Harley, Impact of the biophysical features of a 3D gelatin microenvironment on glioblastoma malignancy. *J. Biomed. Mater. Res. A* **101**, 3404–3415 (2013). doi:10.1002/jbm.a.34637 Medline

62. S. T. Koshy, R. M. Desai, P. Joly, J. Li, R. K. Bagrodia, S. A. Lewin, N. S. Joshi, D. J. Mooney, Click-Crosslinked Injectable Gelatin Hydrogels. *Adv. Healthc. Mater.* **5**, 541–547 (2016). doi:10.1002/adhm.201500757 Medline

63. P. A. Madurantakam, I. A. Rodriguez, C. P. Cost, R. Viswanathan, D. G. Simpson, M. J. Beckman, P. C. Moon, G. L. Bowlin, Multiple factor interactions in biomimetic mineralization of electrospun scaffolds. *Biomaterials* **30**, 5456–5464 (2009). doi:10.1016/j.biomaterials.2009.06.043 Medline

64. G. A. Calderon, P. Thai, C. W. Hsu, B. Grigoryan, S. M. Gibson, M. E. Dickinson, J. S. Miller, Tubulogenesis of co-cultured human iPS-derived endothelial cells and human mesenchymal stem cells in fibrin and gelatin methacrylate gels. *Biomater. Sci.* **5**, 1652–1660 (2017). doi:10.1039/C7BM00223H Medline

65. S. March, E. E. Hui, G. H. Underhill, S. Khetani, S. N. Bhatia, Microenvironmental regulation of the sinusoidal endothelial cell phenotype in vitro. *Hepatology* **50**, 920–928 (2009). doi:10.1002/hep.23085 Medline

66. A. A. Chen, D. K. Thomas, L. L. Ong, R. E. Schwartz, T. R. Golub, S. N. Bhatia, Humanized mice with ectopic artificial liver tissues. *Proc. Natl. Acad. Sci. U.S.A.* **108**, 11842–11847 (2011). doi:10.1073/pnas.1101791108 Medline

67. P. O. Seglen, Preparation of isolated rat liver cells. *Methods Cell Biol.* **13**, 29–83 (1976). doi:10.1016/S0091-679X(08)61797-5 Medline

68. J. C. Dunn, R. G. Tompkins, M. L. Yarmush, Long-term in vitro function of adult hepatocytes in a collagen sandwich configuration. *Biotechnol. Prog.* **7**, 237–245 (1991). doi:10.1021/bp00009a007 Medline